Deciphering the radio-star formation correlation on kpc scales. III. Radio-dim and bright regions in spiral galaxies

B. Vollmer, M. Soida, R. Beck, J. D. P. Kenney

A&A 677, A104 (2023)
https://doi.org/10.1051/0004-6361/202346609

Astronomy & Astrophysics

Deciphering the radio–star formation correlation on kpc scales

III. Radio-dim and bright regions in spiral galaxies

B. Vollmer[1], M. Soida[2], R. Beck[3], and J. D. P. Kenney[4]

[1] Université de Strasbourg, CNRS, Observatoire Astronomique de Strasbourg, UMR 7550, 67000 Strasbourg, France
e-mail: bernd.vollmer@astro.unistra.fr
[2] Astronomical Observatory, Jagiellonian University, ul. Orla 171, 30-244 Kraków, Poland
[3] Max-Planck-Institut für Radioastronomie, Auf dem Hügel 69, 53121 Bonn, Germany
[4] Yale University Astronomy Department, PO Box 208101, New Haven, CT 06520-8101, USA

Received 6 April 2023 / Accepted 16 July 2023

ABSTRACT

The relation between the resolved star formation rate (SFR) per unit area and the nonthermal radio continuum emission is studied in 21 Virgo cluster galaxies and the two nearby spiral galaxies, NGC 6946 and M 51. For the interpretation and understanding of our results, we used a 3D model where star formation, 2D cosmic-ray (CR) propagation, and the physics of synchrotron emission are included. Based on the linear correlation between the SFR per unit area and the synchrotron emission and its scatter, radio-bright and radio-dim regions can be robustly defined for our sample of spiral galaxies. We identified CR diffusion or streaming as the physical causes of radio-bright regions of unperturbed symmetric spiral galaxies as NGC 6946. The enhanced magnetic field in the region of interstellar medium (ISM) compression via ram pressure is responsible for the southwestern radio-bright region in NGC 4501. We identified the probable causes of radio-bright regions in several galaxies as CR transport, via either gravitational tides (M 51) or galactic winds (NGC 4532) or ram pressure stripping (NGC 4330 and NGC 4522). Three galaxies are overall radio dim: NGC 4298, NGC 4535, and NGC 4567. Based on our model of synchrotron-emitting disks, we suggest that the overall radio-dim galaxies have a significantly lower magnetic field than expected by equipartition between the magnetic and turbulent energy densities. We suggest that this is linked to the difference between the timescales of the variation in the SFR and the small-scale dynamo. In NGC 4535, shear motions increase the total magnetic field strength via the induction equation, which leads to enhanced synchrotron emission with respect to the SFR in an otherwise radio-dim galactic disk. Radio-bright regions frequently coincide with asymmetric ridges of polarized radio continuum emission, and we found a clear albeit moderate correlation between the polarized radio continuum emission and the radio/SFR ratio. When compression or shear motions of the ISM are present in the galactic disk, the radio-bright regions are linked to the commonly observed asymmetric ridges of polarized radio continuum emission and represent a useful tool for the interaction diagnostics. The magnetic field is enhanced (as observed in NGC 4535 and NGC 4501) and ordered by these ISM compression and shear motions. Whereas the enhancement of the magnetic field is rather modest and does not significantly influence the radio-SFR correlation, the main effect of ISM compression and shear motions is the ordering of the magnetic field, which significantly affects the CR transport. Cosmic-ray energy losses and transport also affect the spectral index, which we measured between 4.85 and 1.4 GHz. The influence of CR losses and transport on the spectral index distribution with respect to the synchrotron/SFR ratio is discussed with the help of model calculations. Based on our results, we propose a scenario for the interplay between star formation, CR electrons, and magnetic fields in spiral galaxies.

Key words. galaxies: interactions – galaxies: ISM – galaxies: magnetic fields – radio continuum: galaxies

1. Introduction

Relativistic particles, or cosmic rays (CRs), and magnetic fields are important components of the interstellar medium (ISM) in galaxies. Cosmic rays are dynamically coupled to the thermal gas, can drive outflows, and modify the structure of shocks. They are the dominant source of ionization and a major source of heating in regions of high surface densities. Moreover, CRs and magnetic fields provide pressure support to the ISM. Cosmic-ray electrons spiralling around magnetic field lines emit synchrotron emission, which can easily be detected in the classical radio domain.

One of the tightest correlations in astronomy is the relation between the integrated radio continuum (synchrotron) and the FIR emission (Helou et al. 1985; Condon 1992; Mauch & Sadler 2007; Yun et al. 2001; Bell 2003; Appleton et al. 2004; Kovács et al. 2006; Murphy et al. 2009; Sargent et al. 2010; Li et al. 2016). It holds over five orders of magnitude in various types of galaxies including starbursts. The common interpretation of the correlation is that both emission types are proportional to star formation: the radio emission via (i) the CR source term which is due to supernova explosions and the turbulent amplification of the small-scale magnetic field (small-scale dynamo, see, for example, Schleicher & Beck 2013) and (ii) the FIR emission via the dust heating mainly through massive stars. Within nearby galaxies, variations in the radio-FIR correlation have been observed by Gordon et al. (2004), Hughes et al. (2006), Murphy et al. (2006, 2008), Dumas et al. (2011), and Tabatabaei et al. (2013a,b).

Gordon et al. (2004) found variations of $q = \log(\mathrm{FIR}/3.75 \times 10^{-12}\,\mathrm{Hz}) - \log(S_{1.49\,\mathrm{GHz}})$ on the order of 1 dex in M 81. The variation in q was found to be coherent with structures related to the spiral arms, confirming that the radio-infrared (IR) correlation is more complex inside individual galaxies than between galaxies.

Hughes et al. (2006) found that the slope of the relation between the radio and FIR emission is nonlinear in the Large Magellanic Cloud (LMC). In bright star-forming regions, the radio emission increases faster than it does linearly with respect to the FIR emission (power-law slope of ∼1.2), whereas a flatter slope of ∼0.6–0.9 applies more generally across the LMC.

Dumas et al. (2011) also found a large scatter in the resolved radio–24 µm correlation of the galactic disk of M 51. The radio–24 µm ratio presents a complex behavior with local extrema corresponding to various galactic structures, such as complexes of HII regions, spiral arms, and interarm filaments, indicating that the contribution of the thermal and nonthermal radio emission is a strong function of environment. In particular, the relation of the resolved 24 µm and 20 cm emission presents a linear relation within the spiral arms and globally over the galaxy, while it deviates from linearity in the interarm and outer regions ($R > 7.5$ kpc) as well in the inner region ($R < 1.6$ kpc).

Tabatabaei et al. (2013a) investigated the correlation between the IR and free-free–synchrotron radio continuum emission at 20 cm from the two local group galaxies M 31 and M 33 on spatial scales between 0.4 and 10 kpc. They found that the synchrotron-IR correlation is stronger in M 33 than in M 31 on small scales (<1 kpc), but it is weaker in M 31 on larger scales. They argued that the difference on small scales can be explained by the smaller CR propagation length in M 33 than in M 31 and the difference on large scales is due to the thick disk-halo in M 33, which is absent in M 31. Moreover, Tabatabaei et al. (2013b) found that the slope of the radio-FIR correlation across NGC 6946 varies as a function of the star formation rate (SFR) and the magnetic field strength.

For the integrated correlation between the nonthermal 20 cm continuum emission (RC) and the SFR in 17 nearby spiral galaxies, Heesen et al. (2014) found $RC \propto SFR^{1.11\pm0.08}$. The locally averaged correlation between the RC emission and SFR tracers in pixels of 1.2 and 0.7 kpc resolution yielded a slope 0.63 ± 0.25. These authors argue that diffusion of CR electrons is responsible for flattening the local radio–SFR relation, resulting in a sublinear relation.

Cosmic-ray electrons are produced in supernova remnants. Before losing their energy by synchrotron radiation, CR electrons propagate significantly farther via diffusion or streaming than the mean-free path of dust-heating photons. Murphy et al. (2006) tested a phenomenological model that describes the radio continuum image as a smeared version of the FIR image. They found that galaxies with higher IR surface brightnesses have substantially shorter best-fit smoothing scale lengths than those for lower surface brightness galaxies. Murphy et al. (2008) decomposed the IR images into one component containing the star-forming structures and a second one for the diffuse disk. The components were then smoothed separately. They found that the disk component dominates for galaxies having low star formation activity, whereas the structure component dominates at high star formation activity.

Berkhuijsen et al. (2013) studied the radio–SFR correlation in M 31 and M 33 and found sublinear slopes. They convolved the thermal radio continuum map, assuming it to be a representation of the star formation surface density, with a Gaussian kernel, so that the nonthermal radio–SFR relation becomes linear, and used this as an estimate for the CR diffusion length (see also Heesen et al. 2014).

Vollmer et al. (2020) obtained predicted radio continuum maps of Virgo cluster spiral galaxies by convolving the maps of CR electron sources, represented by that of the star formation, with adaptive Gaussian and exponential kernels. The ratio between the smoothing lengthscales at 6 cm and 20 cm could be used to determine, between diffusion and streaming, which is the dominant transport mechanism; whereas the diffusion lengthscale is proportional to $\nu^{-0.25}$, the streaming lengthscale is proportional to $\nu^{-0.5}$, where ν is the frequency. The dependence of the smoothing lengthscale on the SFR contains information on the dependence of the magnetic field strength on the SFR, or the ratio between the ordered and turbulent magnetic field strengths on the SFR. These authors found that perturbed spiral galaxies tend to have smaller lengthscales, which is a natural consequence of the enhancement of the magnetic field caused by the interaction probably via large-scale ISM compression.

For the present study, we took an approach to investigate the physics governing the resolved radio–SFR correlation, which is different from our previous work (Vollmer et al. 2020). Rather than convolving the SFR maps with Gaussian or exponential kernels, as we did in our previous work, for this work we directly calculated the ratio between the resolved nonthermal radio continuum emission and the SFR to identify radio-bright and radio-dim regions within the galaxies. In this way we avoided the artificial smoothing of sharp edges in the radio continuum distribution, which are naturally produced by ram pressure in cluster galaxies (for example, Vollmer et al. 2007). In addition, we compared the radio/SFR ratios to the spectral index to identify the dominant energy loss and the influence of CR propagation. In a second step, the analytical model for nonthermal synchrotron emission developed by Vollmer et al. (2022) was applied to dynamical simulations, which can be directly compared to our observations.

The structure of this article is the following: the radio, IR, and UV observations and the calculation of the SFR maps are described in Sect. 2. Maps of the radio/SFR ratio in connection with the radio continuum spectral index are presented in Sect. 3. Our model for galactic synchrotron emission is introduced and its results are compared to our observations in Sect. 4. Our findings are discussed in Sect. 5 and we give our conclusions in Sect. 6.

2. Observations

For the radio continuum maps we used published VLA data at 4.85 and 1.4 GHz at 15–22″ resolution for all galaxies. The Virgo spiral galaxies were observed at 4.85 GHz between November 8, 2005 and January 10, 2006 and between October 12, 2009 and December 23, 2009 with the Very Large Array (VLA) of the National Radio Astronomy Observatory (NRAO) in the D array configuration. The band passes were 2×50 MHz. We used 3C286 as the flux calibrator and 1254+116 as the phase calibrator, the latter of which was observed every 40 min. Maps were made for both wavelengths using the AIPS task IMAGR with ROBUST = 3. The final cleaned maps were convolved to a beam size of 18″ × 18″ (Vollmer et al. 2010) or 22″ × 22″ (Vollmer et al. 2013). In addition, we observed the galaxies at 1.4 GHz on August 15, 2005 and on March 21, 2008 in the C array configuration. The band passes were 2×50 MHz. We used the same calibrators as for the 4.85 GHz observations. The final cleaned maps were convolved to a beam size of 20″ × 20″ (Vollmer et al. 2010) or 22″ × 22″ (Vollmer et al. 2013)

In addition, we used VLA 4.85 and 1.4 GHz images of NGC 4254 (Chyży et al. 2007), NGC 6946 (Beck 2007), and M 51 (Fletcher et al. 2011) with spatial resolutions of 15″ × 15″. NGC 6946 and M 51 are nearby nearly face-on spiral galaxies with clear spiral structure (plus a tidal interaction for M 51), that show clear trends between the radio-SFR ratio and galaxy

Table 1. Galaxy sample.

Name	D (Mpc)	i (deg)	$S_{4.85\,\mathrm{GHz}}$ (mJy)	$S_{1.4\,\mathrm{GHz}}$ (mJy)	SFR ($M_\odot\,\mathrm{yr}^{-1}$)	$\log(M_*)$ ($M_\odot$)
NGC6946	7.7	38	480	1400	3.5	10.5
M51	8.6	20	400	1300	2.9	10.6
NGC4254	17	30	162.0	510.0	3.6	10.4
NGC4294	17	70	11.5	32.3	0.3	9.2
NGC4298	17	57	8.0	24.8	0.4	10.1
NGC4299	17	22	7.7	17.6	0.3	9.5
NGC4302	17	90	13.2	43.2	0.5	10.4
NGC4303	17	25	135.1	398.5	3.6	10.5
NGC4321	17	27	99.1	256.0	3.2	10.7
NGC4330	17	90	4.7	13.3	0.1	9.5
NGC4396	17	72	8.3	15.8	0.2	9.3
NGC4402	17	74	26.3	68.0	0.5	10.0
NGC4419	17	74	9.2	17.7	0.6	10.2
NGC4457	17	33	16.2	34.1	0.4	10.4
NGC4501	17	57	96.2	331.0	2.3	11.0
NGC4522	17	79	7.6	24.0	0.1	9.4
NGC4532	17	70	51.2	119.9	0.8	9.2
NGC4535	17	43	28.7	66.0	1.6	10.5
NGC4567/68	17	49/66	46.8	128.8	1.8	9.92/10.33
NGC4579	17	38	43.3	88.4	0.8	10.9
NGC4654	17	51	49.9	134.6	1.7	10.1
NGC4808	17	68	19.4	62.6	0.7	9.5

morphology/ISM substructure (Tabatabaei et al. 2013a; Dumas et al. 2011). We subtracted strong point sources and the thermal free-free radio emission according to the recipe of Murphy et al. (2008)

$$\left(\frac{S_{\mathrm{therm}}}{\mathrm{Jy}}\right) = 7.9\times10^{-3}\left(\frac{T}{10^4\,\mathrm{K}}\right)^{0.45}\left(\frac{\nu}{\mathrm{GHz}}\right)^{-0.1}\left(\frac{I_\nu(24\,\mu\mathrm{m})}{\mathrm{Jy}}\right), \quad (1)$$

where T is the electron temperature and $I_\nu(24\,\mu\mathrm{m})$ is the flux density at a wavelength of 24 µm. We note that there are other alternative methods to account for the thermal free-free emission using, for example, the extinction-corrected Hα emission (Tabatabaei et al. 2007; Heesen et al. 2014). We define the spectral index SI as $I_\nu \propto \nu^{-\mathrm{SI}}$. In the following, the term radio continuum emission denotes the nonthermal or synchrotron component of the resolved radio continuum emission.

The star formation rate was calculated from the FUV luminosities corrected by the total IR to FUV luminosity ratio (Hao et al. 2011). This method takes into account the UV photons from young massive stars which escape the galaxy and those which are absorbed by dust and reradiated in the FIR:

$$\dot{\Sigma}_* = 8.1\times10^{-2}\,(I(\mathrm{FUV}) + 0.46\,I(\mathrm{TIR})), \quad (2)$$

where I(FUV) is the GALEX far ultraviolet and I(TIR) the total IR intensity based on *Spitzer* IRAC and MIPS data in units of MJy sr^{-1}. $\dot{\Sigma}_*$ has the units of $M_\odot\,\mathrm{kpc}^{-2}\,\mathrm{yr}^{-1}$. This prescription only holds for a constant star formation rate over the last few 100 Myr. The recipes for the calculation of the TIR emission together with comments on the validity of different star formation estimators are given in Appendix A.

The integrated SFR, the radio continuum flux at 4.85 GHz from Vollmer et al. (2010, 2013), and the stellar mass from Boselli et al. (2015) of each galaxy are presented in Table 1.

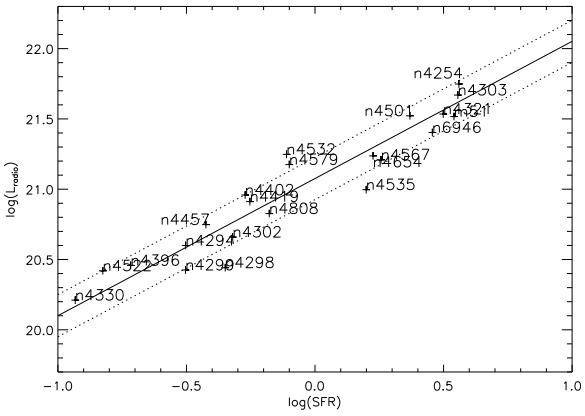

Fig. 1. Radio luminosity at 4.85 GHz in W Hz^{-1} as a function of the star formation rate in $M_\odot\,\mathrm{yr}^{-1}$. The black line represents the result of a outlier-resistant linear regression with a slope of 1.0, the dotted lines the scatter of 0.15 dex.

The integrated radio luminosities at 4.85 GHz as a function of the integrated star formation rates for our sample galaxies are shown in Fig. 1.

The slope of the $\log(L_{\mathrm{rad}})$–$\log(\mathrm{SFR})$ relation is 1.00 with a scatter of 0.15 dex. Many of the perturbed Virgo cluster galaxies (NGC 4522, NGC 4457, NGC 4402, NGC 4532, NGC 4501, and NGC 4254) are located at the upper end of the observed range of radio luminosities with respect to the SFR. On the other hand, NGC 4298 and NGC 4535 have radio luminosities about 2σ or a factor of about two lower than expected based on their SFR.

3. Results

For the spatially resolved correlations we show one data point per resolution element (15−22″). The resolved correlation

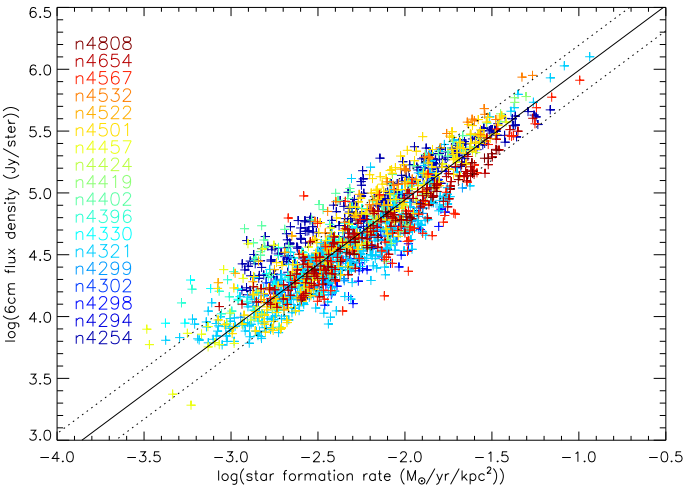

Fig. 2. Resolved properties measured in 15−22″ apertures. Radio continuum surface brightness at 4.85 GHz as a function of the star formation rate per unit area. The black line represents the result of a outlier-resistant linear regression with a slope of 1.05, the dotted lines the scatter of 0.20 dex.

between the 100 µm surface brightness $I_{100\,\mu m}$ and the 4.85 GHz radio continuum surface brightness $I_{4.85\,GHz}$ is presented in Fig. B.1. Only galaxies for which *Herschel* 100 µm data are available are shown. The radio surface brightness distributions of NGC 4303, NGC 4535, and NGC 4579 significantly deviate from the mean relation over the whole disk regions and were excluded from the outlier-resistant linear regression. NGC 4535 is overall radio-dim (see Sect. 4.5) and the radio continuum emission within the disk of NGC 4579 probably has a strong AGN contribution (see Sect. 3.1). The slope of the $\log(I_{100\,\mu m})$–$\log(I_{4.85\,GHz})$ relation is 1.02 with a scatter of 0.17 dex.

The resolved correlation between the SFR per unit area $\dot{\Sigma}_*$ and the 4.85 GHz radio continuum surface brightness $I_{4.85\,GHz}$ is presented in Fig. 2. As for the 100 µm data, galaxies whose radio continuum surface brightness significantly deviates from the mean were excluded (NGC 4303, NGC 4535, and NGC 4579). The slope of the $\log(\dot{\Sigma}_*)$–$\log(I_{4.85\,GHz})$ relation is 1.05 with a scatter of 0.20 dex. This result implies that $\dot{\Sigma}_*$ and $I_{100\,\mu m}$ show a very strong correlation. The slopes of the $\log(\dot{\Sigma}_*)$–$\log(I_{4.85\,GHz})$ relations of the individual galaxies are given in Table F.2.

3.1. Radio-bright and radio-dim regions

We used the results of the linear regression of Fig. 2 to define radio-bright ($\log(I_{4.85\,GHz}) > \log(I_{exp}) + 0.25$) and radio-dim regions ($\log(I_{4.85\,GHz}) < \log(I_{exp}) - 0.25$). I_{exp} is the expected surface brightness from the linear fit of Fig. 2. Radio-bright and radio-dim regions are thus defined on an absolute scale, which is justified by the tightness of the resolved radio–SFR correlation. The second, third and fourth columns of Fig. 3 show the star formation rate per unit area, the star formation rate per unit area (contours) on the ratio between the radio continuum surface brightness and the star formation rate per unit area (color), and the radio continuum surface brightness (contours) on the radio-dim (red) and radio-bright (blue) regions.

The ratio between the resolved radio continuum emission and the SFR depends on the fraction of thermal electrons, CR losses, CR propagation (diffusion, streaming, advection), and radio active galactic nucleus (AGN) components. CRs can move relative to the ISM by streaming along magnetic field lines down a CR density gradient. Advection means the common transport of CRs together with the ISM and the associated magnetic field. Vertical advection of CR electrons can lead to CR escape and/or thick radio disks or halos in disk galaxies (for example, Krause et al. 2018). Moreover, ram pressure can push CR electrons and magnetic fields out of the galactic plane (for example, Vollmer et al. 2021a). The ratio between the resolved radio continuum emission and the SFR also depends on the frequency of the radio continuum observations via the synchrotron lifetime of the CR electrons, which increases for decreasing frequency:

$$t_{sync} \simeq 4.5 \times 10^7 \left(\frac{B}{10\,\mu G}\right)^{-3/2} \left(\frac{\nu}{GHz}\right)^{-1/2} \text{yr}. \quad (3)$$

In addition, CR electrons can lose their energy via bremsstrahlung, inverse Compton (IC) scattering, ion, and pion production.

To estimate these losses we assumed a stationary CR electron density distribution ($\partial n/\partial t = 0$; Eq. (9)) and that the source term of CR electrons is proportional to the star formation rate per unit volume $\dot{\rho}_*$. For the energy distribution of the CR electrons the standard assumption is a power law with index $-q$, which leads to a power law of the radio continuum spectrum with index $(1 - q)/2$ (for example, Beck 2015). Under these assumptions, the synchrotron emissivity is given by the density per unit energy interval of the primary CR electrons, where E is the energy, $n_0 \propto \dot{\rho}_* t_{eff}$, and

$$\epsilon_\nu d\nu \propto \dot{\rho}_* t_{eff} E^{-q} \frac{E}{t_{sync}} dE \quad (4)$$

(Vollmer et al. 2022). The effective lifetime of synchrotron-emitting CR electrons t_{eff} is set by by the synchrotron t_{sync}, bremsstrahlung t_{brems}, IC t_{IC}, ion t_{ion}, and pion t_π loss timescales. Moreover, CR electrons can escape from the galactic disk via vertical diffusion or outflows t_{escp}:

$$\frac{1}{t_{eff}} = \frac{1}{t_{sync}} + \frac{1}{t_{escp}} + \frac{1}{t_{brems}} + \frac{1}{t_{IC}} + \frac{1}{t_{ion}} + \frac{1}{t_\pi}. \quad (5)$$

Whereas a small synchrotron timescale (Eq. (3)) leads to an increase of the synchrotron emission, smaller timescales of bremsstrahlung, IC, ionization, or pion losses lead to a decrease of synchrotron emission. In addition, CR electrons are transported toward regions of low SFR by diffusion or streaming. This decreases the synchrotron emission in regions of high SFR and increases the synchrotron emission in regions of low SFR.

All these effects affect the synchrotron spectral index, which we measured between 4.85 and 1.4 GHz. The comparison between the radio/SFR ratio and the spectral index thus contains information on the physical processes affecting the CR electrons (first row of Fig. 3 where we only show our diagnostic plots for the nearby spiral galaxies NGC 6946 and M 51. The corresponding plots for the Virgo cluster galaxy sample are presented in Figs. C.1–C.4). In Sect. 3.5 we discuss the link between the spectral index distribution and the radio-bright/radio-dim regions. We also produced the diagnostic plots for the 1.4 GHz data (Figs. D.2–D.6). The results are qualitatively similar to those for the 4.85 GHz data, albeit the radio/SFR–SI correlation is significantly stronger at 1.4 GHz compared to the correlation at 4.85 GHz. Since our 4.85 GHz observations have a much better UV coverage because of the much longer observation times, we preferred to use and discuss these data.

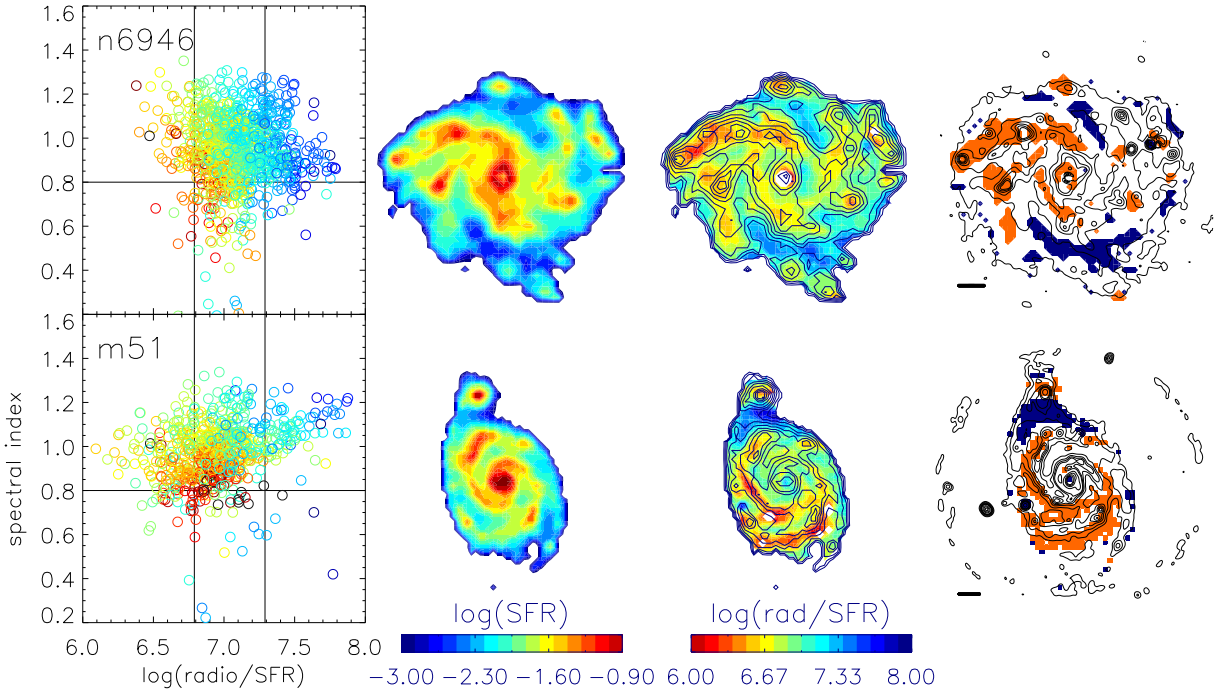

Fig. 3. Relation between the spectral index and radio-bright and radio-dim regions. From left to right: (i) spectral index as a function of the ratio between the radio surface brightness and the star formation rate per unit area, the colors correspond to the star formation rate per unit area (red corresponds to high values); (ii) star formation rate per unit area ($M_\odot$ kpc^{-2} yr^{-1}); (iii) star formation rate per unit area (contours) on the ratio between the radio continuum surface brightness (Jy/sr) and the star formation rate per unit area (color); (iv) radio continuum surface brightness (contours) on the radio-dim (red) and radio-bright (blue) regions. The radio continuum contour levels are (1, 2, 4, 6, 8, 10, 20, 30, 40, 50)× 200 μJy beam^{-1}. The horizontal lines correspond to a size of 1′.

The observed local radio/SFR ratios range from 0.4 dex to 1.4 dex, which corresponds to about 5 times the scatter of the overall correlation (Fig. 2). Even if there is an imbalance between radio-dim or radio-bright regions, the integrated radio/SFR ratio is not strongly affected (Fig. 1) because these regions do not prevail. Even if NGC 4501 and NGC 4522 show radio-bright regions and lie above the integrated radio–SFR correlation, their radio flux densities are still within the scatter (0.15 dex) of the correlation. The radio-dim and radio-bright regions thus represent a second order effect to the radio–SFR correlation. As shown by Vollmer et al. (2022) the losses of Eq. (5) are most relevant for the integrated radio–SFR correlation.

The radio-bright regions in NGC 6946 (Fig. 3) correspond to the interarm regions and are thus most probably caused by CR diffusion or streaming. The radio-bright region in M 51 (Fig. 3) is located toward NGC 5195 and is thus most probably due to CR advection via gravitational tides. Indeed, the atomic hydrogen has a relatively high surface density in this region (Walter et al. 2008). On the other hand, the HI velocity dispersion outside the spiral arm is quite high in the radio-bright region, which might have led to an increase of the magnetic field. The one-sided radio-bright regions in NGC 4330 (Fig. C.2) and NGC 4522 (Fig. C.3) coincide with stripped extraplanar gas (Vollmer et al. 2006, 2012, 2021a) and are thus due to CR transport together with the interstellar medium (ISM) via ram pressure. The one-sided radio-bright region in NGC 4402 (Fig. C.2) might correspond to stripped gas (Crowl et al. 2005) or a radio halo or a thick radio disk (Krause et al. 2018), which has been pushed toward the galactic disk in the south and/or be due to CR transport together with the ISM via ram pressure. In the former scenario one would expect a radio-bright southern edge of the galactic disk due to compression. Since this is not observed, we prefer the latter scenario. The southern radio-bright region in NGC 4501 (Fig. C.3) coincides with a region of ISM compression caused by ram pressure (Vollmer et al. 2008). This might also be the case for the southern radio-bright region in NGC 4254 (Fig. C.1; Chyży et al. 2007), the other radio-bright regions being probably caused by shear motions that were revealed by Phookun et al. (1993) or by CR diffusion or streaming. The radio-bright region in NGC 4532 (Fig. C.3) is extended in the polar direction and shows a strong poloidal magnetic field component visible in polarized emission (Vollmer et al. 2013). Therefore, this region is most probably due to a nuclear starburst outflow.

The radio-bright region in NGC 4579 (Fig. C.4) is enigmatic. Since a CR source (the AGN), which is not connected to star formation, is probably involved in NGC 4579 (Appendix E), we discarded this galaxy when we calculated sample-average values.

The radio-dim regions in all galaxies can be due to (i) CR diffusion or streaming out of regions of high SFR or (ii) bremsstrahlung, IC, ionization, pion, or escape losses. We refer to Sect. 3.5 for further discussion with respect to the spectral index. Three galaxies are overall radio-dim: NGC 4298 (Fig. C.1), NGC 4535, and NGC 4567 (Fig. C.4). NGC 4567 is not present in Fig. 1 because we did not separate NGC 4567 from NGC 4568 for the integrated data. It is remarkable that two out of three overall radio-dim galaxies are gravitationally interacting (NGC 4298 and NGC 4567).

NGC 4535 has an asymmetric distribution of polarized radio continuum emission in the western half of its disk (Vollmer et al. 2007), which coincides with strong shear motions detected in the HI velocity field (Chung et al. 2009). These shear motions are thus responsible for the region of enhanced polarized radio

continuum emission. Within this region the radio/SFR ratio is normal, that is it is enhanced with respect to the otherwise radio-dim galactic disk. We argue that the shear motions increase the ordered magnetic field strength via the induction equation and hence also the total magnetic field strength.

3.2. Correlations

The synchrotron radio/SFR ratio can be modified by CR transport or a change in the magnetic field strength. The magnetic field strength might be enhanced by ISM shear or compression motions, which are traced by the polarized radio continuum emission (Vollmer et al. 2007, 2010, 2013).

To identify the causes of the variations of the radio/SFR ratio, we investigated the relations between the SFR and (i) radio continuum, (ii) polarized emission (PI), and (iii) fractional polarization (FP) and (iv) the radio continuum emission and the polarized emission. For each of these four relations we calculated the Spearman rank correlation coefficients (Table F.1) and the slopes (Table F.2) of the log-log relations via a Bayesian approach to linear regression with errors in both directions (Kelly 2007). The detailed results on these correlations are presented in Appendix F.

The three basic correlations are SFR–radio, SFR–PI, and radio–PI with slopes of 1.11 ± 0.02, 0.43 ± 0.03, and 0.41 ± 0.02, respectively[1]. The SFR–radio correlation is much steeper and tighter than the SFR–PI correlation resulting in an SFR–FP anti-correlation. The difference of the SFR–radio, SFR–PI slopes is -0.83 ± 0.04, which corresponds to the measured SFR–FP slope. The radio–FP slope follows directly from the radio–PI slope.

3.3. The SFR–radio/SFR and PI–radio/SFR relations

To further identify the causes of the variations of the radio/SFR ratio, we investigated if the local radio/SFR ratio depends on the SFR per unit area. Only a weak anticorrelation was found between these two quantities for the whole sample (Spearman rank correlation coefficient $\rho = -0.29$; Fig. 4). Only NGC 6946, NGC 4254, and NGC 4654 show strong anticorrelations ($\rho < -0.6$).

We realized that the radio-bright regions frequently coincide with the asymmetric ridges of polarized radio continuum emission presented in Vollmer et al. (2010, 2013) and regions of enhanced polarized radio continuum emission, which does not follow the spiral structure. These regions are clearly different from classical interarm regions with high polarization. In the eight galaxies presented in Fig. 5 regions of high polarized radio continuum emission coincide at least partly with radio-bright regions. Since the inverse is not always true, other mechanisms than enhanced polarized emission can lead to radio-bright regions.

The asymmetric regions of enhanced polarized emission are located in the outer disks of NGC 4254 (south), NGC 4303 (ring-like), NGC 4396 (west), NGC 4457 (east), NGC 4501 (south-west), and NGC 4535 (west); they are located in the inner parts of the disks in NGC 4532 and NGC 4579. In the two latter galaxies, the enhanced total power and polarized radio continuum emission is due to an outflow (starburst and AGN, respectively).

To investigate the relationship between polarization and radio-brightness, we correlated the local radio/SFR ratios with the surface brightness of polarized radio continuum emission for the 11 individual galaxies (Fig. 6) and for the sample of 11 galaxies (lower right panel of Fig. G.1).

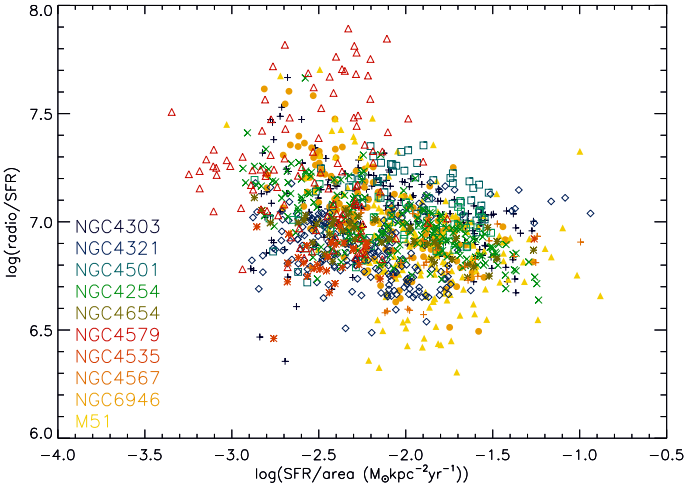

Fig. 4. Ratio between the radio surface brightness (Jy/sr) and the star formation rate per unit area ($M_\odot$ pc^{-2} yr^{-1}) as a function of the star formation rate per unit area.

The corresponding Spearman rank correlation coefficients ρ are presented in the seventh column of Table F.1. Moderate correlations ($0.4 \lesssim \rho \lesssim 0.6$) are found in most galaxies, except for NGC 6946, NGC 4254, and NGC 4654. The strongest correlation is found in the southern compressed region of NGC 4501 ($\rho = 0.62$). The slopes of the subset of moderately correlating log(PI)–log(radio/SFR) relations (seventh column of Table F.2) vary between 0.33 and 0.50. Only the log(PI)–log(radio/SFR) relation of NGC 4579 has an exceptional slope of 1.08. The Spearman rank correlation coefficient for the whole sample is $\rho = 0.41$ and the slope is 0.31. If we remove NGC 6946, NGC 4254, and NGC 4654 from the sample, the correlation coefficient and slope become 0.51 and 0.36 ± 0.03, respectively. We thus observe a clear albeit moderate correlation between the surface brightness of polarized radio continuum emission and the radio/SFR ratio (see Appendix G for a detailed discussion of the correlation). This correlation is consistent with an enhancement and ordering of the magnetic field in regions of ISM compression and shear motions.

The two perturbed galaxies NGC 4254 and NGC 4654, which show a weak or absent correlation between the surface brightness of polarized radio continuum emission and the radio/SFR ratio, present a moderate or strong ($\rho > 0.5$) correlation between the fractional polarization (FP) and the radio/SFR ratio (second column of Table F.2). The slopes of these correlations (Fig. H.1) range between 0.12 and 0.42. The FP–radio/SFR correlation of NGC 6946 is very weak ($\rho = 0.3$) but significantly higher than the PI-radio/SFR correlation. It is remarkable that, except for the isolated galaxy NGC 6946, the radio/SFR ratio is correlated with either FP or PI. In the latter galaxy, the FP–radio/SFR relation is significantly stronger than that of the PI–radio/SFR relation. The two correlations thus seem to be exclusive.

3.4. Interpretation

Polarized synchrotron intensity at high radio frequencies (to avoid Faraday depolarization) measures the ordered magnetic field projected on the plane of the sky within the telescope beam. A regular (or coherent) field has a well-defined direction

[1] The slopes were determined for the combined data of all galaxies except NGC 4579.

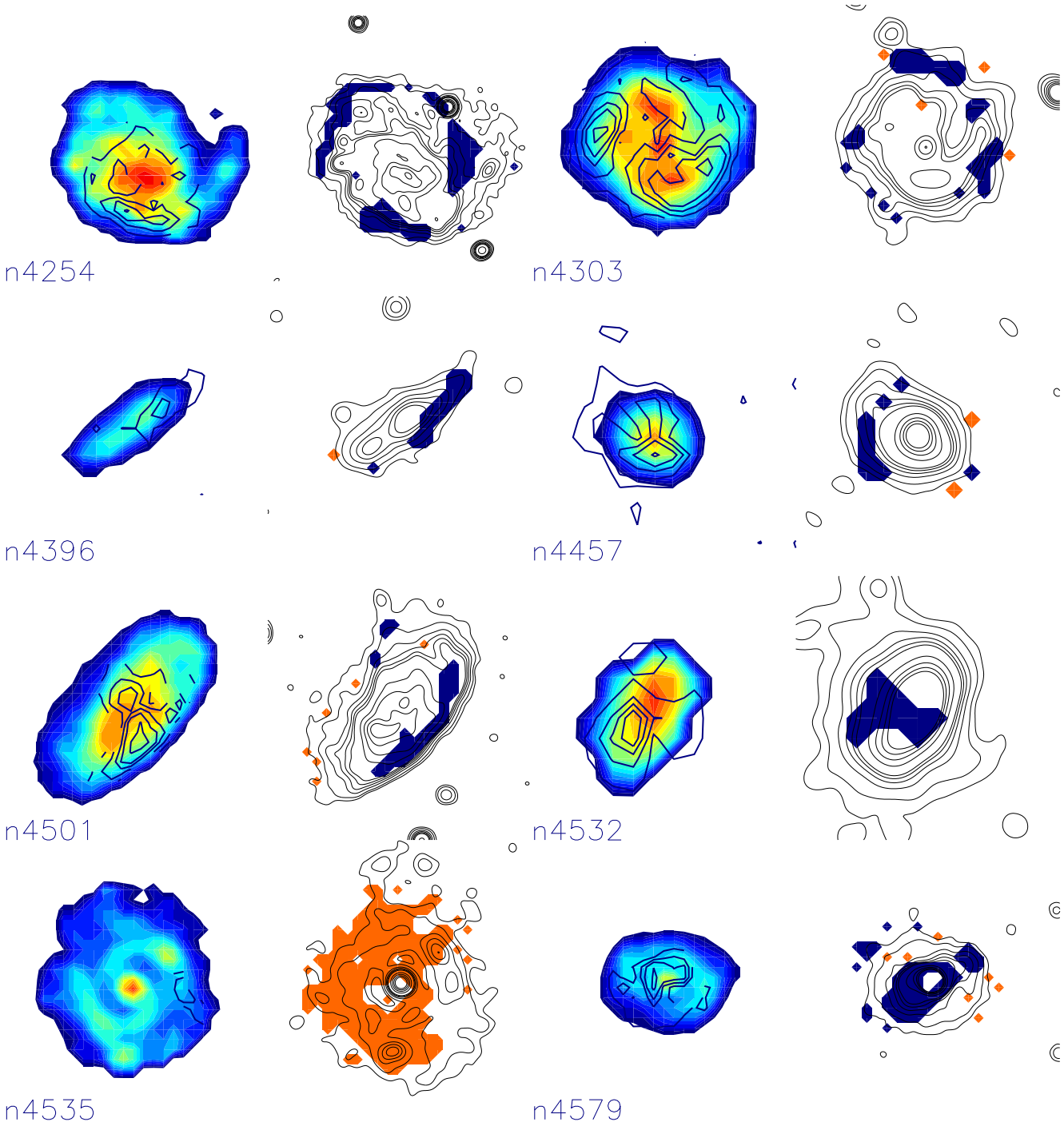

Fig. 5. Relation between polarization and radio-bright and radio-dim regions. For each galaxy: left panel: polarized intensity (contours) on the star formation rate per unit area (color); right panel: radio continuum surface brightness (contours) on the radio-dim (red) and radio-bright (blue) regions. For the color and contour levels we refer to Appendix C.

within the beam of the telescope. Turbulent magnetic fields can be isotropic (i.e., the same dispersion in all three spatial dimensions) or anisotropic (i.e., different dispersions; Beck et al. 2019). In the latter case local field fluctuations are not isotropic but rather prefer certain orientations (not directions; Jaffe 2019). The ordered field is made of the regular and anisotropic field components. In general, the ordered magnetic field component is dominated by the anisotropic field component (Table 3 of Beck et al. 2019).

For the interpretation of our findings we assume the following framework: CR electrons are created in supernova shocks, which are located in starforming region within the galactic disk. These CR electrons undergo mainly synchrotron losses, bremsstrahlung, and IC losses in regions of high SFR and diffuse or stream from regions of high SFR to regions of low SFR. Since there are no starburst galaxies[2] in our sample, escape losses via galactic winds are not important. The isotropic random magnetic field is created by a small-scale dynamo. It is enhanced (as

[2] NGC 4532, which is located slightly above the main-sequence of starforming galaxies (Renzini & Peng 2015), has an outflow that is radio-bright.

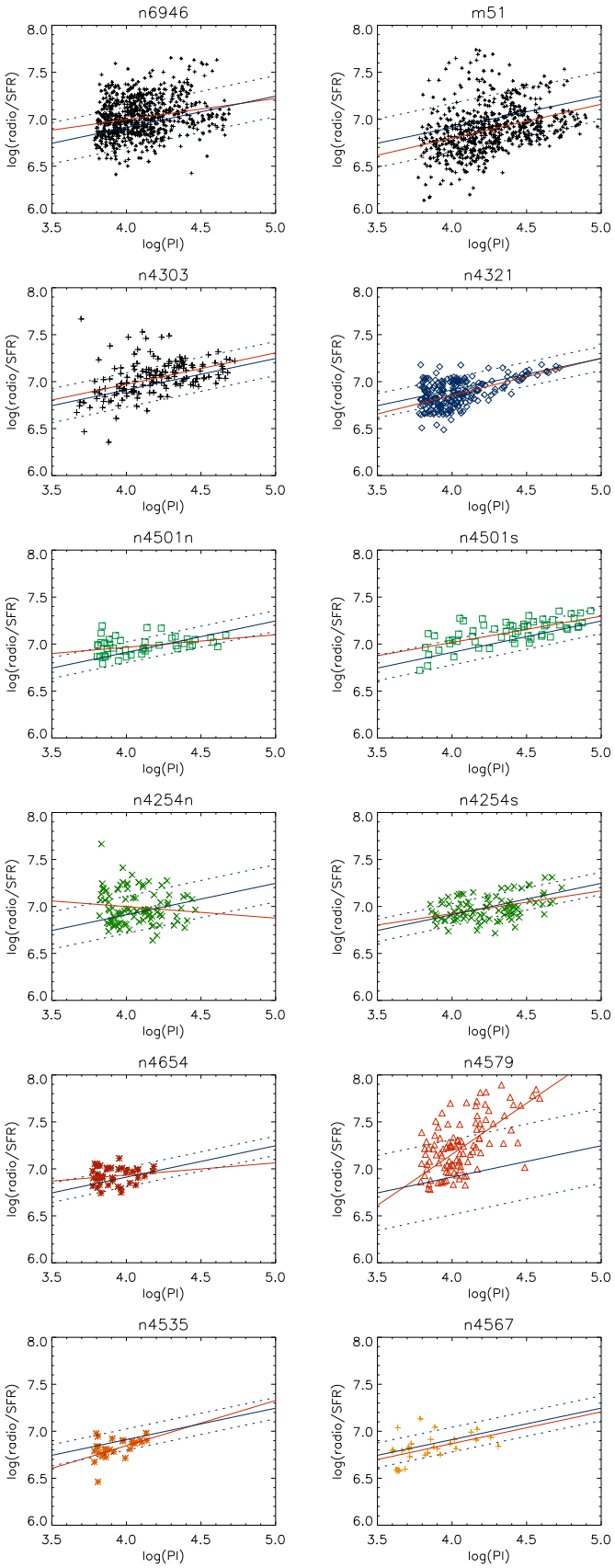

Fig. 6. Ratio between the radio surface brightness and the star formation rate per unit area as a function of the polarized intensity. The blue lines show the common linear fit and scatter for the relation of all Virgo galaxies except NGC 4579, the red lines show the individual linear fits for each galaxy.

observed in NGC 4535 and NGC 4501) and becomes anisotropic by ISM compression and shear motions in perturbed regions of galactic disks. In addition, the large-scale dynamo creates a regular field component in regions of low SFR, i.e. the interarm regions. This regular field might dominate the total field in the so-called magnetic arms (for example, Beck et al. 2019). The regular field is tangled in regions of high star formation rates where the turbulent energy density is high.

In the simulations of Seta & Federrath (2020), the small-scale, random field (with zero mean and nonzero rms) was generated by the tangling of the nonzero mean field due to turbulence. Energetically, the input turbulent kinetic energy was converted into small-scale magnetic energy by shredding of the mean field (the second term on the right hand side of their Eq. (8)). This mean field was maintained by the large-scale dynamo and held constant due to periodic boundary conditions in these simulations.

A discussion on the log(SFR)–log(radio) and log(SFR)–log(FP) correlations can be found in Appendix H. We suggest that the SFR–FP correlation in all galaxies is driven by the fact that the large-scale dynamo operates preferably in regions with low SFR (see, for example, Beck et al. 2019). Moreover, the steeper slopes of the SFR–FP correlation are caused by compression and shear of isotropic random fields (which lead to anisotropy via field ordering), which mainly occur in regions with low SFR where the gas energy density is also low.

Shear affects the magnetic field geometry if the kinetic energy density due to shear is larger than that of the turbulent gas

$$\rho v_{\rm turb} l_{\rm driv} R \frac{\partial \Omega}{\partial R} > \rho v_{\rm turb}^2, \tag{6}$$

where $v_{\rm turb}$ is the turbulent velocity dispersion, $l_{\rm driv}$ the turbulent driving length scale, R the galactic radius, Ω the angular rotation velocity, and ρ the gas density. For a constant rotation curve this leads to

$$t_{\rm shear} = \left(R \frac{\partial \Omega}{\partial R} \right)^{-1} \sim \Omega^{-1} < t_{\rm turb} = \frac{l_{\rm driv}}{v_{\rm turb}}. \tag{7}$$

For typical values of $l_{\rm driv} \sim 100\,{\rm pc}$ and $v_{\rm turb} \sim 10\,{\rm km\,s^{-1}}$ the turbulent timescale is $t_{\rm turb} \sim 10\,{\rm Myr}$. For a spiral arm width of 500 pc (Velusamy et al. 2015) a velocity difference of about $50\,{\rm km\,s^{-1}}$ is needed for shear leading to field ordering. Such high shear velocities are not observed in symmetric spiral arms. On the other hand, such a velocity difference is observed in the western gas arm of NGC 4535 (Chung et al. 2009).

Similarly, compression leads to magnetic field ordering if the compression timescale is smaller than the turbulent timescale

$$t_{\rm comp} = \rho \left(\frac{\partial \rho}{\partial t} \right)^{-1} < t_{\rm turb}. \tag{8}$$

We note that the compression timescale is smaller in regions with low gas densities. The bridge region of the Taffy galaxies (Vollmer et al. 2021b) or the large-scale shock region in Stephan's Quintet (Nikiel-Wroczyński et al. 2013) might be examples of large-scale ICM compression with associated radio continuum polarization. The compression timescale cannot be derived from observations but from simulations (Vollmer et al. 2021b). A future project will be devoted to this issue. Here we suggest that Eq. (8) is fulfilled in parts of the southwestern compressed gas of NGC 4501.

We conclude that in NGC 4535 and NGC 4501 the radio continuum emission in the sheared and compressed regions

is enhanced with respect to the radio continuum emission of the rest of the disk. Thus shear and compression lead to field ordering and a locally enhanced total magnetic field via the induction equation. We argue that the observed PI–radio/SFR correlation is caused by magnetic field enhancement and ordering via ISM shear and compression motions in the interacting galaxies (Sect. 3.3).

Finally, we ascribe the higher Spearman coefficients and steeper slopes of the radio–PI relation with respect to the SFR–PI relation to the influence of (i) the CR bremsstrahlung and IC losses (Eq. (5)), which are higher in regions of high SFR, and (ii) diffusion or streaming of CR electrons: CR electrons diffuse or stream out of the regions of high SFR and low PI into regions of low SFR and high PI.

3.5. Tying in the spectral index

As stated in Sect. 3.1, the CR energy losses of Eq. (5) affect the synchrotron spectral index, which we measured between 4.85 and 1.4 GHz. Pure synchrotron losses lead to a synchrotron spectral index of $-q/2$. Whereas bremsstrahlung, ionization, and pion losses lead to a flatter spectrum, IC losses lead to a steeper spectrum (see Fig. I.1). CR transport removes CR electrons from regions of high SFR without changing the spectrum. On the other hand, the CR electrons that were transported into regions of low SFR will age. Since CR electrons of higher energies have smaller synchrotron energy loss times than CR electrons of lower energies, aging leads to a steeper spectrum. The spectral index distributions of NGC 6946 and M 51 are shown in the left panels of Fig. 3, those of the Virgo cluster galaxies in the corresponding figures of Appendix C). Within these plots, the horizontal line corresponds a spectral index (SI) of 0.8 and the vertical lines to the limits of radio-bright and radio-dim regions (Sect. 3.1). The colors correspond to the SFR per unit area with red being high values of SFR/area.

In all galaxies but NGC 4501 and NGC 4532, the resolution elements with the highest SFR per unit area ($\gtrsim 3 \times 10^{-2}\,M_\odot\,\mathrm{kpc}^{-2}\,\mathrm{yr}^{-1}$) have SI around a value of 0.8. Most frequently, the resolution elements with lower SFR per unit area have steeper SI. The vast majority of resolution elements with the lowest SFR per unit area ($\dot{\Sigma}_* \lesssim 3 \times 10^{-3}\,M_\odot\,\mathrm{kpc}^{-2}\,\mathrm{yr}^{-1}$) have SI > 0.8. In NGC 4396 all resolution elements, in NGC 4321, NGC 4522, NGC 4535, NGC 4579, and NGC 4654 some resolution elements with $\dot{\Sigma}_* \lesssim 3 \times 10^{-3}\,M_\odot\,\mathrm{kpc}^{-2}\,\mathrm{yr}^{-1}$ have SI < 0.8. In particular, we observe a clear gradient in the radio/SFR–SI space in NGC 6946, M 51, NGC 4254, NGC 4303, NGC 4396, NGC 4501, NGC 4522, and NGC 4567/68: regions with a low radio/SFR ratio have the shallowest SI (∼0.8). The other 13 galaxies show a vertical distribution of points in the radio/SFR–SI space. The SI distributions in the radio-dim regions of the overall radio-dim galaxies show different behaviors: whereas these regions show a steep SI in NGC 4298, they have shallow SI in NGC 4567 and a broad range of SI in NGC 4535. Lastly, the two nearest galaxies, NGC 6946 and M 51, show quite different log(radio/SFR)–SI distributions: whereas the resolution elements with $\dot{\Sigma}_* \gtrsim 3 \times 10^{-2}\,M_\odot\,\mathrm{kpc}^{-2}\,\mathrm{yr}^{-1}$ are distributed more vertically in NGC 6946, they are distributed more horizontally in M 51. Furthermore, the radio-bright regions in M 51 have significantly steeper SI ($\gtrsim$1.0) than those in NGC 6946 (SI $\lesssim$ 1.0; left panels of Fig. 3).

NGC 4330, NGC 4402, NGC 4522, NGC 4532, and M 51 are clear cases of CR particle advection via ICM ram pressure, galactic winds, or gravitational tides (Sect. 3.1). The CR electrons, which were transported out of the galactic disk will age leading to a steep radio continuum spectrum with SI > 0.8. Indeed, this effect is observed in these five galaxies, which therefore do not need further discussion.

For the other galaxies the interplay between the SFR and radio/SFR ratio on the one hand and the spectral index on the other hand is complex. To understand this interplay, modeling of the synchrotron emission in disk galaxies is needed. A first approach to such a modeling is presented in Sect. 4.

4. Model

For the interpretation and understanding of our results a 3D model, where star formation and the physics of synchrotron emission are included, is highly valuable, as presented in this Section. The CR propagation by diffusion within the disk plane is modeled by the convolution of the model radio continuum image with a symmetric Gaussian kernel, the vertical CR diffusion by an escape timescale. For the calculation of the galaxy dynamics at scales of about ∼1 kpc we used the 3D dynamical model introduced by Vollmer et al. (2001) and applied to NGC 4501 by Vollmer et al. (2008) and Nehlig et al. (2016). For the calculation of the radio continuum emission we used the analytical formalism introduced by Vollmer et al. (2022).

4.1. Dynamical model

The 3D N-body code consists of two components: a non-collisional component that simulates the stellar bulge/disk and the dark halo, and a collisional component that simulates the ISM. A scheme for star formation was implemented where stars were formed during cloud collisions and then evolved as non-collisional particles (see Vollmer et al. 2012). The non-collisional component consists of 81 920 particles that simulate the galactic halo, bulge, and disk. The characteristics of the different galactic components are adapted to the observed properties. We adopted a model where the ISM is simulated as a collisional component, i.e., as discrete particles that possess a mass and a radius and can have inelastic collisions (sticky particles). The 20 000 particles of the collisional component represent gas cloud complexes that evolve in the gravitational potential of the galaxy. During the disk evolution, the particles can have inelastic collisions, the outcome of which (coalescence, mass exchange, or fragmentation) is simplified following Wiegel (1994). This results in an effective gas viscosity in the disk.

As the galaxy moves through the ICM, its clouds are accelerated by ram pressure. Within the galaxy's inertial system, its clouds are exposed to a wind coming from a direction opposite to that of the galaxy's motion through the ICM. The temporal ram pressure profile has the form of a Lorentzian, which is realistic for galaxies on highly eccentric orbits within the Virgo cluster (Vollmer et al. 2001). The effect of ram pressure on the clouds is simulated by an additional force on the clouds in the wind direction. Only clouds that are not protected by other clouds against the wind are affected. Since the gas cannot develop instabilities, the influence of turbulence on the stripped gas is not included in the model. The mixing of the intracluster medium into the ISM is very crudely approximated by a finite penetration length of the intracluster medium into the ISM, i.e., up to this penetration length the clouds undergo an additional acceleration caused by ram pressure. A scheme for star formation was implemented where stars are formed during cloud collisions and then evolve as non-collisional particles. These newly formed star particles carry their time of formation. This star formation scheme reproduces the Schmidt-Kennicutt law (Fig. A.1 of Vollmer et al. 2012).

4.2. Radio continuum emission model

The diffusion–advection–loss equation for the CR electron density n reads as

$$\frac{\partial n}{\partial t} = D\nabla^2 n + \frac{\partial}{\partial E}(b(E)n(E)) - (\boldsymbol{u}+\boldsymbol{v})\nabla n + \frac{p}{3}\frac{\partial n}{\partial p}\nabla \boldsymbol{u} + Q(E) - \frac{n}{t_{\rm loss}}, \quad (9)$$

where D is the diffusion coefficient, E the CR electron energy, $\boldsymbol{u}$ the advective flow velocity, $\boldsymbol{v}$ the streaming velocity, p the CR electron pressure, Q the source term, and $b(E)$ the rate of energy loss. The first part of the right-hand side of Eq. (6) is the diffusion term, followed by the synchrotron loss, advection, streaming, adiabatic energy gain or loss, and the source terms. The advection and adiabatic terms are only important for the transport in a vertical direction. Energy can be lost via inverse Compton (IC) radiation, bremsstrahlung, pion or ionization energy loss, and most importantly synchrotron emission (for example, Murphy et al. 2009; Lacki et al. 2010). Within our basic model we used a constant diffusion coefficient.

Observations of beryllium isotope ratios at the Solar Circle have shown that the confinement timescale for particles ≥3 GeV is dependent on energy (Webber & Higbie 2003). Lacki et al. (2010) use $D(E) \propto \sqrt{E/(3\,\mathrm{GeV})}$ for $E > 3$ GeV. Following Mulcahy et al. (2016), we also tested a constant diffusion coefficient $D = D_0$ for $E \le 3$ GeV and $E = D_0(E/(3\,\mathrm{GeV}))^{\kappa}$ for $E > 3$ GeV. Theoretically predicted values of κ range between 0.3 and 0.6 (Schlickeiser 2002; Shalchi & Schlickeiser 2005; Trotta et al. 2011).

We assumed a stationary CR electron density distribution ($\partial n/\partial t = 0$; Eq. (9)). The CR electrons are transported into the halo through diffusion or advection where they lose their energy via adiabatic losses or where the energy loss through synchrotron emission is so small that the emitted radio continuum emission cannot be detected. Furthermore, we assumed that the source term of CR electrons is proportional to the SFR per unit volume $\dot{\rho}_*$. For the energy distribution of the CR electrons, the standard assumption is a power law with index q, which leads to a power law of the radio continuum spectrum with index $-(q-1)/2$ (for example, Beck 2015). For the synchrotron emissivity we used Eq. (4) with the effective timescale given by Eq. (5).

For the characteristic timescales, we followed the prescriptions of Lacki et al. (2010). The diffusive escape timescale based on observations of beryllium isotope ratios at the solar circle (Connell 1998; Webber et al. 2003) is

$$t_{\rm esc} = 26/\sqrt{E/3\,\mathrm{GeV}}\,\mathrm{Myr} \quad (10)$$

for $E > 3$ GeV and $t_{\rm diff} = 26$ Myr otherwise. The mean energy E is calculated via the mean synchrotron frequency

$$\nu_{\rm s} = 1.3\times10^{-1}\left(\frac{B}{10\,\mu\mathrm{G}}\right)\left(\frac{E}{\mathrm{GeV}}\right)^2\,\mathrm{GHz}. \quad (11)$$

The characteristic time for bremsstrahlung is

$$t_{\rm brems} = 37\left(\frac{n}{\mathrm{cm}^{-3}}\right)^{-1}\,\mathrm{Myr}, \quad (12)$$

and that for IC energy losses is

$$t_{\rm IC} = 180\left(\frac{B}{10\,\mu\mathrm{G}}\right)^{\frac{1}{2}}(\nu_{\rm GHz})^{-\frac{1}{2}}\left(\frac{U}{10^{-12}\,\mathrm{erg\,cm}^{-3}}\right)^{-1}\,\mathrm{Myr}, \quad (13)$$

where U is the interstellar radiation field. The timescale of ionization-energy loss is

$$t_{\rm ion} = 210\left(\frac{B}{10\,\mu\mathrm{G}}\right)^{-\frac{1}{2}}(\nu_{\rm GHz})^{\frac{1}{2}}\left(\frac{n}{\mathrm{cm}^{-3}}\right)^{-1}\,\mathrm{Myr}. \quad (14)$$

The magnetic field strength B is calculated under the assumption of energy equipartition between the turbulent kinetic energy of the gas and the magnetic field:

$$\frac{B^2}{8\pi} = \frac{1}{2}\rho v_{\rm turb}^2, \quad (15)$$

where ρ is the total midplane density of the gas and $v_{\rm turb}$ its turbulent velocity dispersion. Thus, within the framework of the symmetric analytical model the magnetic field is characterized only by its energy density.

With $\nu = CBE^2$, the synchrotron emissivity of Eq. (4) becomes

$$\epsilon_\nu = \xi\dot{\rho}_*\frac{t_{\rm eff}(\nu)}{t_{\rm sync}(\nu)}B^{\frac{q}{2}-1}\nu^{-\frac{q}{2}}. \quad (16)$$

The constant is $C = e/(2\pi m_{\rm e}^2 c^2)$. With the CR electron density $n_0 \propto \dot{\rho}_* t_{\rm eff}$ and Eq. (3), the classical expression $\epsilon_\nu \propto n_0 B^{(q+1)/2}\nu^{(1-q)/2}$ is recovered. In Vollmer et al. (2022) the factor ξ was chosen such that the radio–IR correlations measured by Yun et al. (2001) and Molnár et al. (2021) are reproduced within 2σ (their Fig. 8). We assumed $q = 2.3$ as our fiducial model but also investigated the case of $q = 2.6$. The gas density ρ, turbulent gas velocity dispersion $v_{\rm turb}$, and interstellar radiation field U are directly taken from the dynamical model.

The radio continuum emission map was calculated in the following way:

1. For all gas particles the gas density and velocity dispersion are calculated with the 50 nearest neighbors;
2. The magnetic field strength B is calculated for each gas particle using Eq. (15);
3. The radiation field U is calculated for each star particle using all other star particles that are younger than 10 Myr;
4. The synchrotron and loss timescales are calculated for each star particle;
5. Equation (16) is evaluated for each star particle and added to the model radio continuum map;
6. The model map is convolved with Gaussian kernels of size $l = 2\sqrt{D\,t_{\rm eff}}$ with $D = 10^{28}\,\mathrm{cm}^2\,\mathrm{s}^{-1}$; in this way vertical diffusion within the galactic disk was neglected;
7. The projection angles are applied to the model map.

In the following the escape timescale is neglected. Its influence is described in Appendix I. For the synchrotron emission, bremsstrahlung and IC losses are most important. Ionization and pion losses are less important but cannot be neglected (Fig. I.1). We intentionally did not calibrate the units of the SFR per unit area and the radio continuum surface brightness because we mainly used their ratio and the spectral index, which does not depend on units.

4.3. Large-scale magnetic field model

To calculate the large-scale regular magnetic field for our simulations, we followed the same procedure as Soida et al. (2006). Time- dependent gas-velocity fields provided by the 3D dynamical simulations were used as input for solving the dynamo (induction) equation using a second-order Godunov scheme with second-order upstream partial derivatives together with a

second-order Runge-Kutta scheme for the time evolution. To avoid nonvanishing $\nabla \cdot \boldsymbol{B}$, we evolved the dynamo equation expressed by the magnetic potential A, where $\boldsymbol{B} = \nabla \times \boldsymbol{A}$, ($\boldsymbol{B}$ is the magnetic induction):

$$\frac{\partial \boldsymbol{B}}{\partial t} = \nabla \times (\boldsymbol{v} \times \boldsymbol{B}) - \nabla \times (\eta \nabla \boldsymbol{B}), \quad (17)$$

where $\boldsymbol{v}$ is the large-scale velocity of the gas, and η the coefficient of a turbulent diffusion. We assumed the magnetic field to be partially coupled to the gas via the turbulent diffusion process (Elstner et al. 2000) whilst assuming the magnetic diffusion coefficient to be $\eta = 3 \times 10^{25}$ cm^2 s^{-1}. We did not implement any explicit dynamo process. The resulting polarized emission is calculated by assuming a density of relativistic electrons that is proportional to the model gas density ρ. This rather crude approximation is motivated by the fact that in quiescent galaxies, the density of relativistic electrons is approximately proportional to the star formation density which depends on $\rho^{1-1.7}$. These calculations permit to determine the geometry of the large-scale magnetic field but not its strength.

4.4. Model results

For the comparison with observations three characteristic models were calculated: a symmetric model, a perturbed model with one-sided compressed ISM, and a model with a globally radio-dim galactic disk.

4.4.1. Symmetric model

For our basic model we used a timestep of the NGC 4654 simulations presented in Lizée et al. (2021). NGC 4654 is perturbed by a rapid flyby of a spherical galaxy with a mass of $9.2 \times 10^{10}\,M_\odot$. At the time of interest the perturber is located at a distance of 18.9 kpc. It will reach its minimum distance of 18.3 kpc within ~20 Myr. We chose this particular timestep because the galaxy developed marked spiral arms being still symmetric.

For the calculation of the synchrotron emission we set the exponent of the energy distribution of CR particles to $q = 2.3$ (Eq. (4)). As a first model we set $t_{\rm eff} = t_{\rm sync}$, i.e. there are no other than synchrotron losses. CR diffusion is absent. The resulting radio–SFR relation and SI as a function of the radio/SFR ratio are shown in the left column of Fig. 7. The log(radio)–log(SFR) correlation has a slope of 1.08 and a scatter of 0.02 dex. As expected, the spectral index is constant SI = 1.15.

We then set $t_{\rm eff}^{-1} = t_{\rm brems}^{-1} + t_{\rm IC}^{-1} + t_{\rm ion}^{-1} + t_{\pi}^{-1}$ (middle column of Fig. 7). The log(radio)–log(SFR) correlation has a slope of 0.89 and the scatter increases to 0.11 dex. We divided the galaxies into radio-bright and radio-dim regions according to the mean and scatter. There is no clear correlation between these regions and the SFR per unit area. It has to be noted that all regions are radio normal if one applies the observed scatter of 0.20 dex.

In the third model we allowed for CR diffusion within the disk plane (right column of Fig. 7). To do so we set the diffusion length to

$$l = \mathrm{diff} = 2\sqrt{D\,t_{\rm eff}}, \quad (18)$$

where we assumed a diffusion coefficient of $D = D_0 = 10^{28}$ cm^2 s^{-1}. This procedure corresponds to an instantaneous diffusion approximation.

Heesen et al. (2019) found $D = (0.13\text{–}1.5) \times 10^{28}$ cm^2 s^{-1} at 1 GeV within three local spiral galaxies. Mulcahy et al. (2016) derived a value of $D = 6.6 \times 10^{28}$ cm^2 s^{-1} for $E < 3$ GeV in M 51. Moreover, the Milky Way diffusion coefficient is $D = 3 \times 10^{28}$ cm^2 s^{-1} (Strong et al. 2007). Vollmer et al. (2020) derived a value of $D = (1.8 \pm 0.6) \times 10^{28}$ cm^2 s^{-1} at ~5 GeV from 6 cm radio continuum data. Our model diffusion coefficient is thus at the lower end of the observationally derived range. Models with a two times higher and an energy-dependent diffusion coefficient ($\kappa = 0.3$) are presented in Fig. I.2. Models with diffusion coefficients $\gtrsim 2 \times 10^{28}$ cm^2 s^{-1} or $\kappa > 0.3$ lead to model radio/SFR–SI relations which are not consistent with our observations.

The log(radio)–log(SFR) correlation has a slope of 0.73 and the scatter increases to 0.23 dex, which is comparable to the observed value of 0.20 dex. We note that the log(radio)–log(SFR) correlation of NGC 6946 has a slope of 0.76 (Table F.2). CR diffusion therefore creates radio-dim and radio-bright regions. As observed, the radio-bright regions mainly coincide with interarm regions. We caution the reader that we only modeled isotropic diffusion. Anisotropic diffusion along the large-scale magnetic field lines will still lead to radio-bright and radio-dim regions but decrease the contrast between these regions. CR diffusion does not increase the spectral index in our model. The only way to significantly increase SI is to increase q. The inclusion of CR streaming where $l = l_{\rm str}$ if $l_{\rm str} > l_{\rm diff}$ (see Vollmer et al. 2020) with $l_{\rm str} = v_{\rm str} t_{\rm eff}$ and $v_{\rm str} = 100$ km s^{-1} leads to a somewhat steeper slope of 0.80. The inclusion of diffusive CR escape increases the slope of the log(radio)–log(SFR) correlation to 0.95 (Fig. I.3).

We conclude that we are able to reproduce the resolved radio/SFR and SI values of a symmetric spiral galaxy as, for example, NGC 6946. Whereas the different CR electron losses lead to the overall level of radio continuum emission and are thus relevant for the integrated radio–SFR correlation (Vollmer et al. 2022), diffusion or streaming lead to the observed radio-bright and radio-dim regions in symmetric spiral galaxies.

4.4.2. Perturbed model

NGC 4501 is a well-studied showcase for almost edge-on ram pressure stripping (Vollmer et al. 2008). The ISM in the southern half of the galactic disk is compressed by ram pressure and shows a high molecular fraction (Nehlig et al. 2016) and a bright asymmetric ridge of polarized radio continuum emission (Vollmer et al. 2007). This region is clearly radio-bright (Fig. C.3). For the comparison with observations we used the dynamical simulations presented in Nehlig et al. (2016). Since this galaxy shows particularly high spectral indices, we set $q = 2.7$ instead of $q = 2.3$. The model results including CR diffusion are presented in Fig. 8.

Even without CR diffusion, the southwestern region of compressed ISM is radio-bright (Δ log(radio/SFR) > 0.25). This is due to the enhanced magnetic field strength in the compressed gas (Eq. (15)). Including CR diffusion steepens the log(SFR)–log(radio) and flattens the log(radio/SFR)–SI distribution. Our diffusion lengths (Eq. (18)) seem to be somewhat overestimated.

The log(SFR)–log(radio) correlation of the model with and without CR diffusion have a slope of 0.84/0.96 and a scatter of 0.25/0.16 dex, respectively. The southwestern compressed region is radio-bright as it is observed (Fig. C.3). However, it is less extended than the observed radio-bright region. The radio-bright region in the southeast is absent in the 4.85 GHz data but present in the 1.4 GHz data. The model distribution of the spectral index with respect to log(radio/SFR) (lower left panel of Fig. 8) is well comparable to the observed distribution (Fig. C.3).

Based on our conclusion that shear motions in NGC 4535 enhance the magnetic field strength via the induction equation

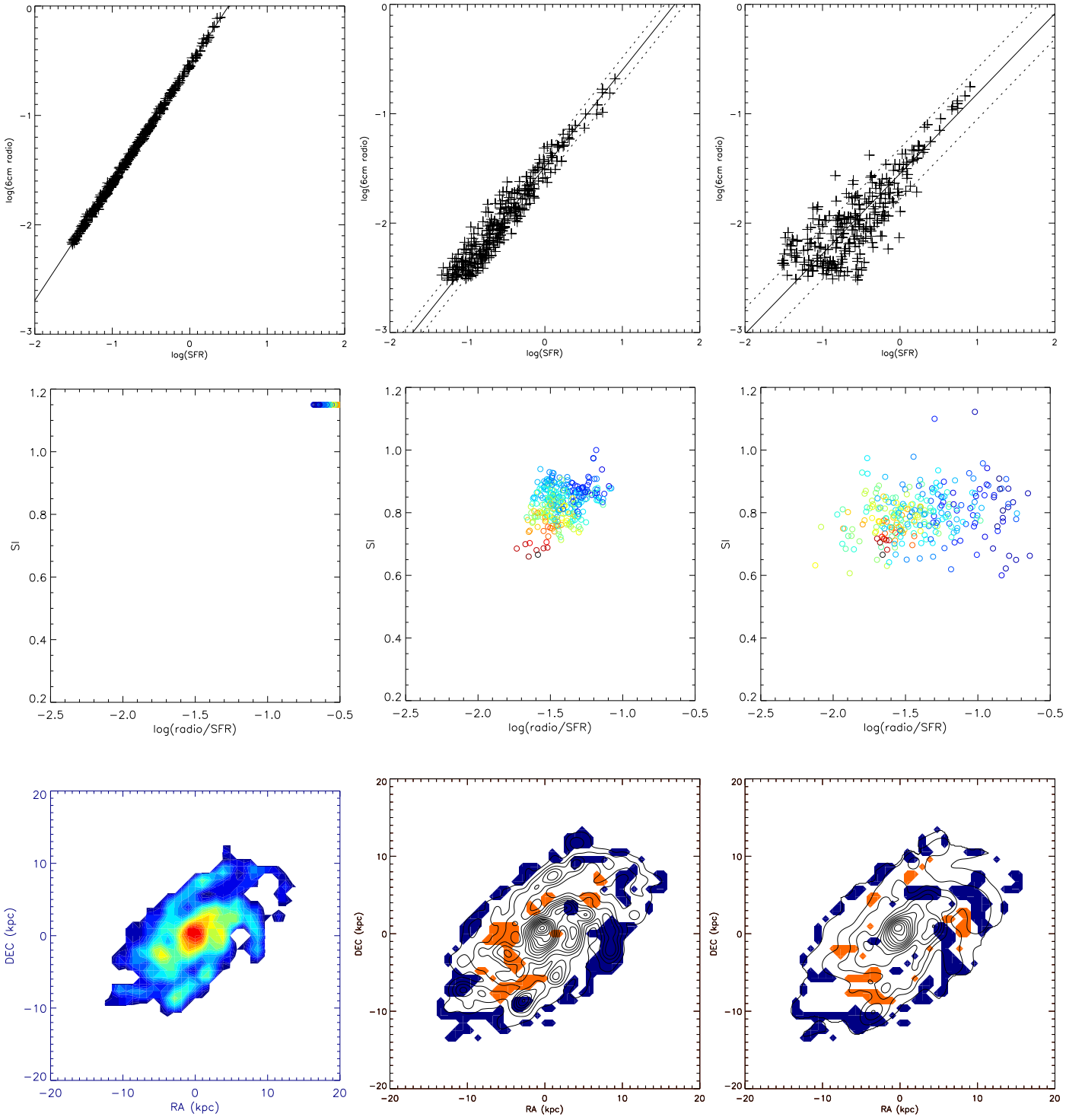

Fig. 7. Model calculations in arbitrary units. Left column: $t_{\rm eff} = t_{\rm sync}$ without diffusion; middle column: $t_{\rm eff}^{-1} = (t_{\rm sync}^{-1} + t_{\rm brems}^{-1} + t_{\rm IC}^{-1} + t_{\rm ion}^{-1} + t_{\pi}^{-1})^{-1}$ without diffusion; right column: with diffusion. Upper row: radio continuum surface brightness at 4.85 GHz as a function of the star formation rate per unit area; middle row: spectral index as a function of the ratio between the radio continuum surface brightness and the star formation rate per unit area; lower row: left: star formation rate per unit area; middle and right: radio continuum surface brightness at 4.85 GHz (contours) on radio-dim (red) and radio-bright (blue) regions.

(Sect. 3), we increased the magnetic field strength by 12 µG in regions of high model polarization (see Sect. 4.3; left panel of Fig. 9). This field strength is comparable to the ordered field in the southern PI ridge of NGC 4501 assuming energy equipartition between the magnetic field and the CR particles and a path-length along the line-of-sight of 2 kpc. In this way we obtained a more extended radio-bright region in the southern half of the galaxy (right panel of Fig. 9). As before, the southwestern region of compressed ISM is radio-bright even without CR diffusion.

For the basic model with CR diffusion the Spearman rank correlation coefficient of the log(FP)–log(radio/SFR) relation and the log(PI)–log(radio/SFR) are 0.08 and 0.55, respectively (upper panels of Fig. I.4). This means that only the polarized radio continuum emission is correlated with the radio/SFR ratio.

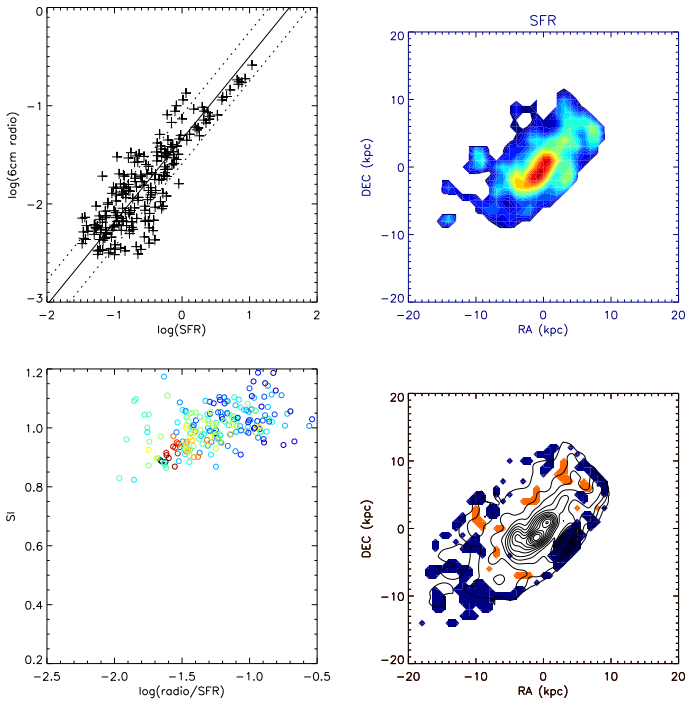

Fig. 8. NGC 4501 model (arbitrary units). Upper left: radio continuum surface brightness at 4.85 GHz as a function of the star formation rate per unit area; upper right: star formation rate per unit area; lower left: spectral index as a function of the ratio between the radio continuum surface brightness and the star formation rate per unit area; lower right: radio continuum surface brightness at 4.85 GHz (contours) on radio-dim (red) and radio-bright (blue) regions.

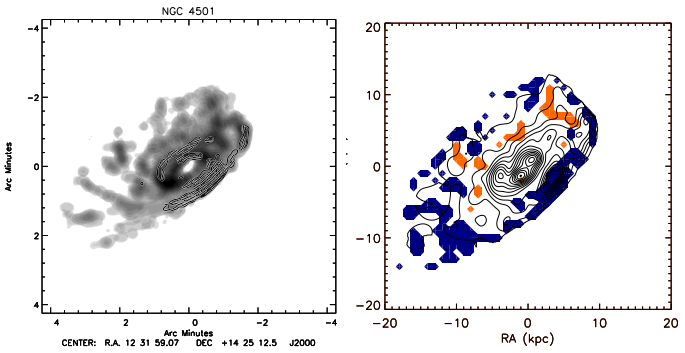

Fig. 9. NGC 4501 model. Left panel: polarized radio continuum emission (contours) with magnetic field vectors on HI emission (gray scale). Right panel: same model as in Fig. 8 but with an additional regular field component $B_{\rm reg}$ = 12 µG in regions of enhanced model polarized intensity. Radio continuum surface brightness at 4.85 GHz (contours) on radio-dim (red) and radio-bright (blue) regions.

The slope of the log(PI)–log(radio/SFR) relation is 0.47. For the model with increased magnetic field strength in regions of high polarized emission the Spearman rank correlation coefficient the log(FP)–log(radio/SFR) relation increases to 0.37, that of the log(PI)–log(radio/SFR) relation decreases to 0.51 (lower panels of Fig. I.4). The slope of the log(PI)–log(radio/SFR) relation decreases to 0.31, which is close to the average of the observed slopes of 0.33. However, we caution against the absence in our model of depolarization effects due to the tangling of the ordered magnetic field by the turbulent motions of the ISM.

We conclude that we can reproduce the observed main characteristics of the perturbed Virgo spiral galaxy NGC 4501: the radio-bright region of compressed ISM and the correlation between the polarized radio continuum emission and the radio/SFR ratio. The radio-bright region is mainly caused by the high magnetic field strength in the compressed ISM. CR diffusion or streaming enhance the radio-brightness and somewhat flatten the radio continuum spectrum within the radio-bright regions.

4.5. Radio-dim galactic disk model

There are three overall radio-dim galaxies in our sample: NGC 4298, NGC 4535, and NGC 4567. Radio-dim model galactic disks can be obtained by a decrease of the magnetic field strength with respect to its equipartition value (Eq. (15)). As an example, we set $B = 0.6 \times \sqrt{4\,\pi\,\rho\,v_{\rm turb}^2}$ in the symmetric model (left panels of Fig. 10). Indeed, the bulk of the disk becomes radio-dim. In a second step we added a vertical escape of CR electron by diffusion (Eq. (10)). As expected, the disk becomes even more radio-dim (right panels of Fig. 10). Remarkably, the log(radio/SFR)–SI distribution becomes vertical as it is observed in NGC 4298 and NGC 4535. In general, vertical CR escape makes the log(radio/SFR)–SI distribution more vertical. Vertical CR escape might thus also be important in many other galaxies and most notably in NGC 4321 (Fig. C.2).

Including diffusive escape together with equipartition between the energy densities of the turbulent gas and the magnetic field leads to a galactic disk, which is only radio-dim in the outer parts ($R \gtrsim 5$ kpc). Therefore, within our model framework diffusive escape does not seem to be sufficient for a globally radio-dim galactic disk as observed in NGC 4298, NGC 4535, and NGC 4567. Diffusive escape is not important in the perturbed spiral galaxies because of their high magnetic field strength.

Within the framework of our model a globally radio-dim galactic disk is obtained by a decrease (~60%) of the magnetic field with respect to its equipartition value. Diffusive escape can enhance the radio-dimness in the outer disk and leads to a vertical log(radio/SFR)–SI distribution. In addition, in galaxies with high SFRs CR advection via a galactic wind is expected to play a role.

5. Discussion

5.1. Radio-deficit regions

In undisturbed galaxies the radio emission extends beyond the associated FIR emission/SF region, due to the diffusion and streaming of the CR electrons. However in many Virgo galaxies the radio emission does not extend beyond the associated FIR emission on the leading sides of ram pressure interactions, apparently because the diffusion and streaming of the CR electrons has been inhibited in this direction. This inhibition is presumably due to a sharp edge of the ISM distribution and an associated magnetic field configuration, in which the magnetic field lines are largely aligned along the leading edge of the gas disk as witnessed by the asymmetric ridges of polarized radio continuum emission (see Sect. 3.3).

The presence of these regions lacking the expected radio emission caused by CR diffusion and streaming can be shown by subtracting the radio map from a model made by smoothing the FIR/SFR distribution by an amount that matches the typical radio behavior in undisturbed galaxies. For many Virgo galaxies,

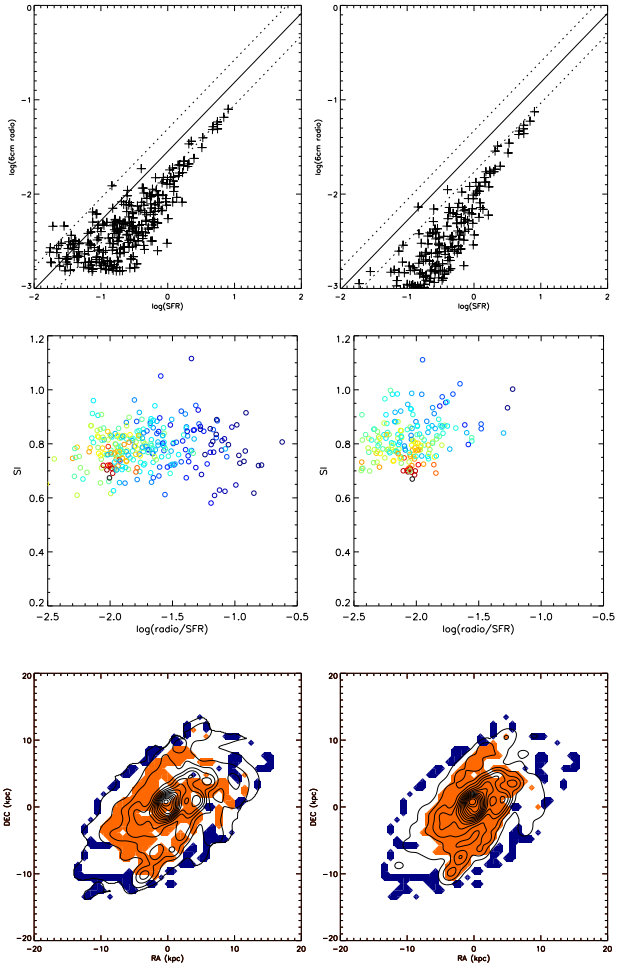

Fig. 10. Model as in Fig. 7 with $B = 0.6\times\sqrt{4\,\pi\,\rho\,v_{\rm turb}^2}$. This model reproduces the globally low radio/SFR ratios in NGC 4298, NGC 4535, and NGC 4567. Left panels: without diffusive escape. Right panels: with diffusive escape.

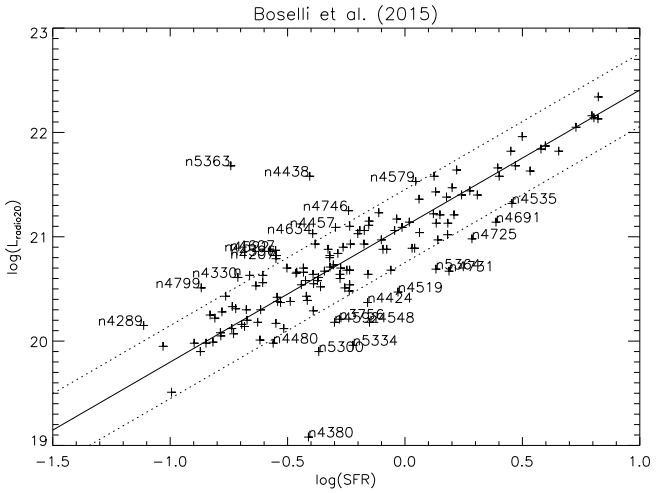

Fig. 11. Radio continuum luminosity at 1.4 GHz as a function of star formation rate for the galaxy sample of Boselli et al. (2015). The solid line represent an outlier-resistant linear regression. The dotted line correspond to to the 1σ scatter.

these difference maps reveal a deficit with respect to the expected radio emission along the side of the outer edge of the gas disk known from other indicators to be the leading side of the ram pressure interaction (Murphy et al. 2009).

We have seven galaxies in common with Murphy et al. (2009): NGC 4254, NGC 4321, NGC 4330, NGC 4396, NGC 4402, NGC 4522, and NGC 4579. These authors found significant radio-deficit regions in NGC 4254, NGC 4330, NGC 4402, and NGC 4522. Since we did not smooth the SF maps in this work, we could not evaluate these deficit regions. Interestingly, we observe low radio/SFR ratios, which we classified as radio-normal though, in the radio-deficit regions of NGC 4330, NGC 4402, and NGC 4522 (Figs. C.1–C.3 and Figs. D.3–D.5).

5.2. FP–PI dichotomy

Within sample of interacting galaxies the radio/SFR ratio is correlated either with the fractional polarization (FP) or polarized radio continuum emission (PI) (Table F.1). We call this the FP–PI dichotomy. This is contrary to expectation that radio/SFR ratio should be correlated to PI if it is correlated with FP. In most galaxies of our sample the radio/SFR ratio correlates with PI. On the other hand, the radio/SFR ratio is only correlated with the SFR ($|\rho| > 0.5$) in NGC 6946, NGC 4254, and NGC 4654 and these are the galaxies where the radio/SFR ratio is best correlated with FP. The SFR–radio/SFR correlation is driven by (i) synchrotron, bremsstrahlung, and IC losses in regions of high SFR and (ii) diffusion or streaming from regions of high SFR to regions of low SFR (see Sect. 4.4.1). Mechanisms (i) and (ii) decrease the radio continuum emission in regions of high SFR. In addition, mechanism (ii) can increase the radio continuum emission in regions of low SFR. Whether the radio continuum emission of low-SFR regions is enhanced depends on the timescale of CR energy losses. The FP–radio/SFR correlation arises because the polarized emission stems from the magnetic field, which is ordered by shear and compression regions related to galactic structure, i.e. spiral arms.

Once the galaxies are significantly perturbed the picture changes: the SFR–radio/SFR correlation is significantly weakened in interacting galaxies where externally triggered shear and compression motions locally enhance the magnetic field and thus the radio continuum emission without significantly affecting the SFR. Within these regions the radio continuum and the polarized emission are enhanced leading to the PI–radio/SFR correlation. As expected, the observed correlation is driven by regions of strong polarized emission.

5.3. Overall radio-dim spiral galaxies

To further investigate the physical reason for a global radio-dimness of spiral galaxies, we show the integrated SFR–radio continuum relation at 1.4 GHz for the sample of Boselli et al. (2015), which is mostly comprised of Virgo spiral galaxies, in Fig. 11.

The slope of the log(SFR)–log(radio) relation is 1.3 with a scatter of 0.27. We identified galaxies with $|\Delta\log(\text{radio/SFR})| > 0.35$ as radio-dim and radio-bright.

By comparing VLA FIRST to NVSS flux densities we found that nine out of 14 radio-bright galaxies seem to be overall radio-bright. Eight out of these nine galaxies are Virgo galaxies. Four out of these eight galaxies are interacting with the intracluster medium (NGC 4330, NGC 4396, NGC 4438, and NGC 4522). NGC 4457 might have had a minor merger in the recent past (Vollmer et al. 2013). As already stated, NGC 4579 is enigmatic: it is an anemic galaxy as NGC 4548, which is

radio-dim, but it is radio-bright probably due to additional radio continuum emission from an AGN-driven outflow (Sect. 3.1). We are thus left with three radio-bright galaxies: NGC 4207, NGC 4289, and NGC 4746. All these galaxies are observed edge-on and are of relatively low mass ($M_* < 5 \times 10^9\,M_\odot$) and have a range of specific star formation rates (sSFR) from normal ($10^{-10}\,\mathrm{yr}^{-1}$) to low ($3 \times 10^{-11}\,\mathrm{yr}^{-1}$).

Out of the 14 radio-dim galaxies six are Virgo galaxies. Thus radio-dimness is not related to the cluster environment. There are two merger remnants (NGC 4691, NGC 4424) and one interacting galaxy (NGC 4731). This is quite surprising because one would expect that gravitational interactions enhance the magnetic fields (Drzazga et al. 2011), but they also enhance the SFR.

We conclude that ongoing hydrodynamic interactions (ram pressure) do whereas ongoing gravitational interaction can enhance the radio emission of disk galaxies. Evolved gravitational interactions can decrease the radio/SFR ratio by up to a factor of about three.

NGC 4548 is a radio-dim anemic gas-poor galaxy with a low sSFR. However, there is a similar galaxy with a normal radio/SFR ratio, NGC 2841 (Heesen et al. 2014). Moreover, the nearby spiral galaxy NGC 3198 is overall radio-dim (Heesen et al. 2014) but otherwise normal (gas content, SFR, sSFR). It thus seems that overall radio-dimness cannot be predicted by any known physical property of a galaxy.

We speculate that the global radio/SFR differences stem from difference between the timescales of (i) the variation in SFR (t_*) and (ii) the small-scale dynamo (t_dynamo). If $t_* > t_\mathrm{dynamo}$, then the galaxy is radio-normal. If the SFR increases and $t_* < t_\mathrm{dynamo}$, the galaxy is radio-deficient (see also Roussel et al. 2003). This is consistent with the fact that two (NGC 4298 and NGC 4567) out of the three overall radio-dim galaxies from Table 1 are parts of interacting pairs. If we interpret the western gas arm of NGC 4535 as sign of an interaction that occurred in the recent past, all three cases are consistent with a scenario where the interaction enhanced the SFR of the galaxies within less time than the timescale of the small-scale dynamo, which is about the turbulent turnover time $\Omega^{-1} = R/v_\mathrm{rot} \sim 100$ Myr. Alternatively, different saturation levels of the galactic small-scale dynamo might also play a role.

6. Summary and conclusions

In this work we have investigated the relation between the resolved SFR per unit area and the nonthermal radio continuum emission. We used the radio continuum observations of 20 Virgo spiral galaxies presented in Vollmer et al. (2010, 2013). For the Virgo spiral galaxy NGC 4254 and the two nearby spiral galaxies NGC 6946 and M 51, we used the radio continuum data from Chyży et al. (2007), Beck (2007), and Fletcher et al. (2011). In addition, we created SFR maps using archival *Spitzer*, *Herschel*, and GALEX data (Sect. 2).

For the interpretation and understanding of our results, we used a 3D model where star formation, CR propagation, and the physics of synchrotron emission are included (Sect. 4). For the calculation of the galaxy dynamics at scales of about ∼1 kpc, we used the 3D dynamical model introduced by Vollmer et al. (2001) and applied to NGC 4501 by Vollmer et al. (2008) and Nehlig et al. (2016). For the calculation of the radio continuum emission, we used the analytical formalism introduced in Vollmer et al. (2022).

The slope of the $\log(I_{100\,\mu\mathrm{m}})$–$\log(I_{4.85\,\mathrm{GHz}})$ relation is 1.02 with a scatter of 0.17 dex, and that of the $\log(\dot{\Sigma}_*)$–$\log(I_{4.85\,\mathrm{GHz}})$ relation is 1.05 with a scatter of 0.20 dex. We used the results of the linear regression of Fig. 2 to define radio-bright ($\log(I_{4.85\,\mathrm{GHz}}) > \log(I_\mathrm{exp}) + 0.25$) and radio-dim regions ($\log(I_{4.85\,\mathrm{GHz}}) < \log(I_\mathrm{exp}) - 0.25$), where I_exp is the expected surface brightness.

The radio/SFR ratio depends on CR energy losses and CR transport. Energy losses decrease the radio continuum emission, whereas CR transport decreases and increases the radio continuum emission in regions with a high and low SFR. Based on our model of synchrotron-emitting disks, we identified CR diffusion or streaming as the physical causes of radio-bright regions of unperturbed symmetric spiral galaxies as NGC 6946 (Sect. 4.4.1). The enhanced magnetic field in the region of ISM compression via ram pressure is responsible for the southwestern radio-bright region in NGC 4501 (Sect. 4.4.2). Cosmic-ray diffusion or streaming enhances the radio-brightness and somewhat flattens the radio continuum spectrum within the radio-bright region. Based on our knowledge of the Virgo spiral galaxies, we identified the physical causes of radio-bright regions: CR advection transport via gravitational tides in M 51, CR transport via a galactic wind in NGC 4532, and CR transport via ram pressure stripping in NGC 4330 and NGC 4522. Three galaxies are overall radio dim: NGC 4298 (Fig. C.1), NGC 4535, and NGC 4567 (Fig. C.4). It is remarkable that two out of three overall radio-dim galaxies are gravitationally interacting (NGC 4298 and NGC 4567).

Based on our model of synchrotron-emitting disks (Sect. 4.5), we suggest that the overall radio-dim galaxies have a significantly lower magnetic field than expected by equipartition between the magnetic and turbulent energy densities (Eq. (15)). We suggest that this is linked to differences between the timescales of the variation in the SFR and the small-scale dynamo. NGC 4535 has an asymmetric distribution of polarized radio continuum emission (Vollmer et al. 2007), which coincides with strong shear motions detected in the HI velocity field (Chung et al. 2009). These shear motions are thus responsible for the region of enhanced polarized radio continuum emission. Within this region, the radio/SFR ratio is normal, that is to say it is enhanced with respect to the otherwise radio-dim galactic disk. We argue that the shear motions increase the total magnetic field strength via the induction equation, which leads to an enhanced radio continuum emission with respect to the SFR.

Radio-bright and radio-dim regions can be robustly defined for our sample of spiral galaxies. Radio-bright regions are caused by CR transport out of their acceleration sites and/or the increase of magnetic field strength via ISM compression or shear motions. In the two latter cases, they are linked to the commonly observed asymmetric ridges of polarized radio continuum emission and represent a useful tool for the interaction diagnostics.

To understand the reasons for the radio-bright and radio-dim regions, we calculated the Spearman rank correlation coefficients and slopes of the resolved SFR–radio, SFR–FP, radio–PI, SFR–PI, PI–radio and SFR, and FP–radio and SFR relations (Sect. 3.2). The three basic correlations are SFR–radio, SFR–PI, and radio–PI with slopes of 1.11, 0.43, and 0.41, respectively. The SFR–radio correlation is much steeper and tighter than the SFR–PI correlation resulting in an SFR–FP anticorrelation. The slope of the SFR–FP correlation is significantly steeper for the interacting galaxies than for NGC 6946. We suggest that the SFR–FP correlation in all galaxies is driven by the action of a large-scale dynamo together with the tangling of regular magnetic fields in regions of relatively high SFR and field ordering by compression and shear motions. The steeper slopes of the SFR–FP correlation in interacting galaxies are caused by

compression and shear of isotropic random fields, which lead to field ordering and mainly occur in regions with a low SFR where the gas energy density is also low.

We realized that the radio-bright regions frequently coincide with the asymmetric ridges of polarized radio continuum emission. In the eight galaxies presented in Fig. 5, radio-bright regions coincide with regions of high polarized radio continuum emission. Indeed, we found a clear, albeit moderate, correlation between PI and the radio/SFR ratio (Fig. G.1). This is consistent with an enhancement and ordering of the magnetic field in regions of ISM compression and shear motions. In our sample galaxies, the radio/SFR ratio is either correlated with PI (in most of the cases) or FP. In galaxies showing a FP–radio and SFR correlation, the radio/SFR ratio is also correlated with the SFR. This correlation is driven by (i) bremsstrahlung and IC losses in regions of high SFR and (ii) diffusion or streaming from regions of high SFR to regions of low SFR (see Sect. 4.4.1).

Cosmic-ray energy losses and transport also affect the spectral index, which we measured between 4.85 and 1.4 GHz. In eight galaxies of our sample, we observed a gradient in radio and SFR–SI space. Diffusion or streaming flatten this gradient and thus lead to a flatter radio continuum spectrum in the radio-bright regions (Sect. 4.4.1). In all other galaxies of our sample, the radio and SFR–SI distribution is vertical. Based on our model of synchrotron-emitting disks (Sect. 4.5), we argue that this vertical distribution is due to diffusive escape of a CR electron in rather weak magnetic fields. The diffusive escape makes the outer parts of the galactic disks radio dimmer (Fig. 10).

We suggest the following scenario for the interplay between star formation, CR electrons, and magnetic fields, which is consistent with our results: CR electrons are created in supernova shocks, which are located in starforming region within the galactic disk. These CR electrons mainly undergo bremsstrahlung and IC losses in regions with a high SFR and diffuse or stream from regions with a high SFR to regions with a low SFR. The isotropic random magnetic field is created by a small-scale dynamo. In addition, the large-scale dynamo creates a regular field component in regions with a low SFR, that is the inter-arm regions. This regular field might dominate the total field in the so-called magnetic arms (for example, Beck et al. 2019). The regular field is tangled and thus destroyed in regions of high SFRs where the turbulent energy density is high. The magnetic field is enhanced (as observed in NGC 4535 and NGC 4501) and ordered by ISM compression and shear motions in spiral arms or perturbed regions of galactic disks. In the perturbed galaxies, the radio/SFR ratio increases slowly with the polarized intensity (radio and SFR $\propto$ PI$^{0.3}$). The enhancement of the magnetic field in regions of ISM compression and shear motions is rather modest and does not significantly influence the radio and SFR correlation. The main effect of compression and shear motions is the ordering of the magnetic field, which can be observed via polarized radio continuum emission.

Acknowledgements. We would like to thank the anonymous referee for careful reading of the manuscript and Amit Seta for useful discussions.

References

Appleton, P. N., Fadda, D. T., Marleau, F. R., et al. 2004, ApJS, 154, 147
Beck, R. 2007, A&A, 470, 539
Beck, R. 2015, A&ARv, 24, 4
Beck, R., & Krause, M. 2005, Astron. Nachr., 326, 414
Beck, R., Chamandy, L., Elson, E., et al. 2019, Galaxies, 8, 4
Bell, E. F. 2003, ApJ, 586, 794
Berkhuijsen, E. M., Beck, R., & Tabatabaei, F. S. 2013, MNRAS, 435, 1598
Boselli, A., Fossati, M., Gavazzi, G., et al. 2015, A&A, 579, A102
Calzetti, D., Wu, S.-Y., Hong, S., et al. 2010, ApJ, 714, 1256
Chung, A., van Gorkom, J. H., Kenney, J. D. P., et al. 2009, AJ, 138, 1741
Chyży, K. T., Ehle, M., & Beck, R. 2007, A&A, 474, 415
Condon, J. J. 1992, ARA&A, 30, 575
Connell, J. J. 1998, ApJ, 501, L59
Crowl, H. H., Kenney, J. D. P., van Gorkom, J. H., et al. 2005, AJ, 130, 65
Daigle, O., Carignan, C., Amram, P., et al. 2006, MNRAS, 367, 469
Davies, J. I., Baes, M., Bendo, G. J., et al. 2010, A&A, 518, L48
Draine, B. T., & Li, A. 2007, ApJ, 657, 810
Drzazga, R. T., Chyży, K. T., Jurusik, W., et al. 2011, A&A, 533, A22
Dumas, G., Mundell, C. G., Emsellem, E., et al. 2007, MNRAS, 379, 1249
Dumas, G., Schinnerer, E., Tabatabaei, F. S., et al. 2011, AJ, 141, 41
Elstner, D., Otmianowska-Mazur, K., von Linden, S., et al. 2000, A&A, 357, 129
Fletcher, A., Beck, R., Shukurov, A., et al. 2011, MNRAS, 412, 2396
Galametz, M., Kennicutt, R. C., Calzetti, D., et al. 2013, MNRAS, 431, 1956
García-Burillo, S., Combes, F., Schinnerer, E., et al. 2005, A&A, 441, 1011
García-Burillo, S., Fernández-García, S., Combes, F., et al. 2009, A&A, 496, 85
Gordon, K. D., Pérez-González, P. G., Misselt, K. A., et al. 2004, ApJS, 154, 215
Hao, C.-N., Kennicutt, R. C., Johnson, B. D., et al. 2011, ApJ, 741, 124
Heesen, V., Brinks, E., Leroy, A. K., et al. 2014, AJ, 147, 103
Heesen, V., Buie, E., Huff, C. J., et al. 2019, A&A, 622, A8
Helou, G., Soifer, B. T., & Rowan-Robinson, M. 1985, ApJ, 298, L7
Helou, G., Roussel, H., Appleton, P., et al. 2004, ApJS, 154, 253
Hughes, A., Wong, T., Ekers, R., et al. 2006, MNRAS, 370, 363
Hummel, E., Krause, M., & Lesch, H. 1989, A&A, 211, 266
Jaffe, T. R. 2019, Galaxies, 7, 52
Kelly, B. C. 2007, ApJ, 665, 1489
Kovács, A., Chapman, S. C., Dowell, C. D., et al. 2006, ApJ, 650, 592
Krause, M., Irwin, J., Wiegert, T., et al. 2018, A&A, 611, A72
Lacki, B. C., Thompson, T. A., & Quataert, E. 2010, ApJ, 717, 1
Leroy, A. K., Walter, F., Brinks, E., et al. 2008, AJ, 136, 2782
Li, J.-T., Beck, R., Dettmar, R.-J., et al. 2016, MNRAS, 456, 1723
Lizée, T., Vollmer, B., Braine, J., et al. 2021, A&A, 645, A111
Mauch, T., & Sadler, E. M. 2007, MNRAS, 375, 931
Molnár, D. C., Sargent, M. T., Leslie, S., et al. 2021, MNRAS, 504, 118
Mulcahy, D. D., Fletcher, A., Beck, R., et al. 2016, A&A, 592, A123
Murphy, E. J., Helou, G., Braun, R., et al. 2006, ApJ, 651, L111
Murphy, E. J., Helou, G., Kenney, J. D. P., et al. 2008, ApJ, 678, 828
Murphy, E. J., Kenney, J. D. P., Helou, G., et al. 2009, ApJ, 694, 1435
Nehlig, F., Vollmer, B., & Braine, J. 2016, A&A, 587, A108
Nikiel-Wroczyński, B., Soida, M., Urbanik, M., et al. 2013, MNRAS, 435, 149
Phookun, B., Vogel, S. N., & Mundy, L. G. 1993, ApJ, 418, 113
Renzini, A., & Peng, Y. 2015, ApJ, 801, L29
Roussel, H., Helou, G., Beck, R., et al. 2003, ApJ, 593, 733
Sargent, M. T., Schinnerer, E., Murphy, E., et al. 2010, ApJ, 714, L190
Seta, A., & Federrath, C. 2020, MNRAS, 499, 2076
Shalchi, A., & Schlickeiser, R. 2005, ApJ, 626, L97
Schleicher, D. R. G., & Beck, R. 2013, A&A, 556, A142
Schlickeiser, R. 2002, Cosmic Ray Astrophysics, Astronomy and Astrophysics Library; Physics and Astronomy Online Library (Berlin: Springer)
Soida, M., Otmianowska-Mazur, K., Chyży, K., et al. 2006, A&A, 458, 727
Sokoloff, D. D., Bykov, A. A., Shukurov, A., et al. 1998, MNRAS, 299, 189
Strong, A. W., Moskalenko, I. V., & Ptuskin, V. S. 2007, Ann. Rev. Nucl. Part. Sci., 57, 285
Tabatabaei, F. S., Beck, R., Krügel, E., et al. 2007, A&A, 475, 133
Tabatabaei, F. S., Schinnerer, E., Murphy, E. J., et al. 2013a, A&A, 552, A19
Tabatabaei, F. S., Berkhuijsen, E. M., Frick, P., et al. 2013b, A&A, 557, A129
Trotta, R., Jóhannesson, G., Moskalenko, I. V., et al. 2011, ApJ, 729, 106
Velusamy, T., Langer, W. D., Goldsmith, P. F., et al. 2015, A&A, 578, A135
Vollmer, B., Cayatte, V., Balkowski, C., et al. 2001, ApJ, 561, 708
Vollmer, B., Soida, M., Otmianowska-Mazur, K., et al. 2006, A&A, 453, 883
Vollmer, B., Soida, M., Beck, R., et al. 2007, A&A, 464, L37
Vollmer, B., Soida, M., Chung, A., et al. 2008, A&A, 483, 89
Vollmer, B., Soida, M., Chung, A., et al. 2010, A&A, 512, A36
Vollmer, B., Soida, M., Braine, J., et al. 2012, A&A, 537, A143
Vollmer, B., Soida, M., Beck, R., et al. 2013, A&A, 553, A116
Vollmer, B., Soida, M., Beck, R., et al. 2020, A&A, 633, A144
Vollmer, B., Fossati, M., Boselli, A., et al. 2021a, A&A, 645, A121
Vollmer, B., Braine, J., Mazzilli-Ciraulo, B., et al. 2021b, A&A, 647, A138
Vollmer, B., Soida, M., & Dallant, J. 2022, A&A, 667, A30
Walter, F., Brinks, E., de Blok, W. J. G., et al. 2008, AJ, 136, 2563
Webber, W. R., & Higbie, P. R. 2003, J. Geophys. Res. (Space Phys.), 108, 1355
Webber, W. R., McDonald, F. B., & Lukasiak, A. 2003, ApJ, 599, 582
Wiegel, W. 1994, Diploma Thesis, University of Heidelberg, Germany
Yun, M. S., Reddy, N. A., & Condon, J. J. 2001, ApJ, 554, 803

Appendix A: Total IR and star formation estimators

The full width at half-maximum (FWHM) of the point spread functions (PSFs), as stated in the *Spitzer* Observer's Manual (*Spitzer* Science Centre 2006), are 1.7, 2.0, 6, and 18 arcsec at 3.6, 8.0, 24, and 70 μm, respectively. In addition, we used *Herschel* Virgo Cluster Survey (HeViCS) 100 and 160 μm images (Davies et al. 2010) which have spatial resolutions of 7 and 12 arcsec, respectively. First, the data are convolved with Gaussian kernels that match the PSFs of the images in the 3.6, 8, 24 70, 100, and 160 μm bands to the PSF of the radio continuum data. Next, the data were re-binned to the common pixel size of the radio continuum maps. We excluded from the analysis regions not detected at the 3σ level in one or more wave bands. This resulted in a loss of surface of 10 % to 20 % compared to the regions with 24 μm 3σ detections with a tendency of less loss for truncated galaxies. Following Helou et al. (2004), we subtracted the stellar continuum from the 8 and 24 μm surface brightnesses (in MJy sr^{-1}) using

$$I_\nu(\mathrm{PAH}\ 8\mu\mathrm{m}) = I_\nu(8\mu\mathrm{m}) - 0.232\ I_\nu(3.6\mu\mathrm{m}) \text{ and} \quad \text{(A.1)}$$

$$I_\nu(24\mu\mathrm{m}) = I_\nu(24\mu\mathrm{m}) - 0.032\ I_\nu(3.6\mu\mathrm{m}). \quad \text{(A.2)}$$

According to the availability of *Spitzer* and *Herschel* data, we calculated the TIR surface brightness in three ways based on Table 3 from Galametz et al. (2013).

1. For NGC 4254, NGC 4294, NGC 4298, NGC 4299, NGC 4302, NGC 4303, NGC 4321, NGC 4330, NGC 4402, NGC 4522, and NGC 4579 we used
$$I(\mathrm{TIR}) = 2.064\ \nu I_\nu(24\mu\mathrm{m}) + 0.539\ \nu I_\nu(70\mu\mathrm{m}) + 0.277\ \nu I_\nu(100\mu\mathrm{m}) + 0.938\ \nu I_\nu(160\mu\mathrm{m})\ ; \quad \text{(A.3)}$$
2. for NGC 6946, M 51, NGC 4396, NGC 4419, NGC 4457, NGC 4532, NGC 4654, and NGC 4808 we used
$$I(\mathrm{TIR}) = 0.95\ \nu I_\nu(8\mu\mathrm{m}) + 1.15\ \nu I_\nu(24\mu\mathrm{m}) + 2.3\ \nu I_\nu(70\mu\mathrm{m})\ ; \quad \text{(A.4)}$$
for NGC 4501, NGC 4535, and NGC 4567/68 we used
$$I(\mathrm{TIR}) = 2.708\ \nu I_\nu(24\mu\mathrm{m}) + 0.734\ \nu I_\nu(100\mu\mathrm{m}) + 0.739\ \nu I_\nu(160\mu\mathrm{m}). \quad \text{(A.5)}$$

In most galactic environments the error introduced to I(TIR) due to incomplete spectral coverage is about 50 %, based on the Draine & Li (2007) models.

The FIR+FUV relation only works for relatively high SFRs (like those in these spiral galaxies, galaxies near 'star-forming main sequence'). For some ellipticals with dust heated by old stars or AGN, this relation gives a huge overestimate of the SFR. Moreover, the SF timescales probed by FIR and GALEX UV might not match – the GALEX UV probes star formation timescales of $\sim$ 50-100 Myr, whereas the FIR probes timescales that are probably shorter, although this depends on the star formation history. Leroy et al. (2008) estimated the typical uncertainty on their 24 μm–FUV star formation rate to be on the order of 50 % or 0.2 dex. The uncertainty of our star formation rates is of the same order. For a comparison between different star formation indicators based on mixed processes (direct stellar light (FUV), dust-processed stellar light (FIR, TIR), ionized gas emission(Hα)) we refer to Calzetti et al. (2010). The total star formation rates obtained with Eq. 2 are about 0.2 dex smaller than those given by Boselli et al. (2015) with a scatter of 0.07 dex.

Appendix B: The 100 μm–4.85 GHz correlation

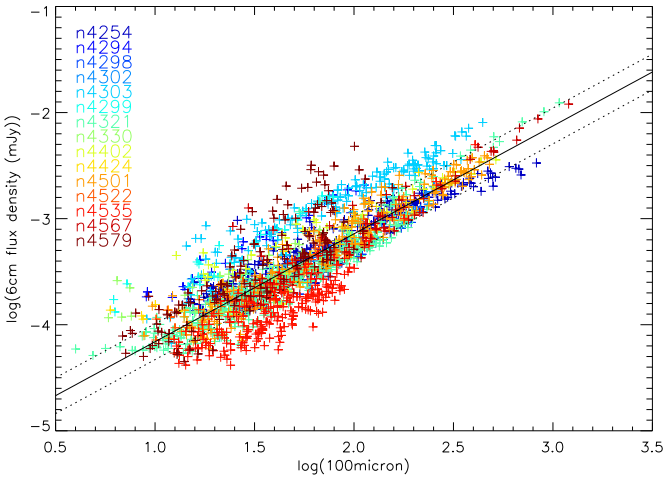

Fig. B.1. Resolved properties measured in 15 – 22″ apertures. Total radio continuum surface brightness at 4.85 GHz as a function of the surface brightness at 100 μm. The black line represents the result of a outlier-resistant linear regression with a slope of 1.02, the dotted lines the scatter of 0.17 dex. NGC 4303, NGC 4535, and NGC 4579 were excluded from the linear regression.

Appendix C: Diagnostic plots for the Virgo cluster galaxy sample

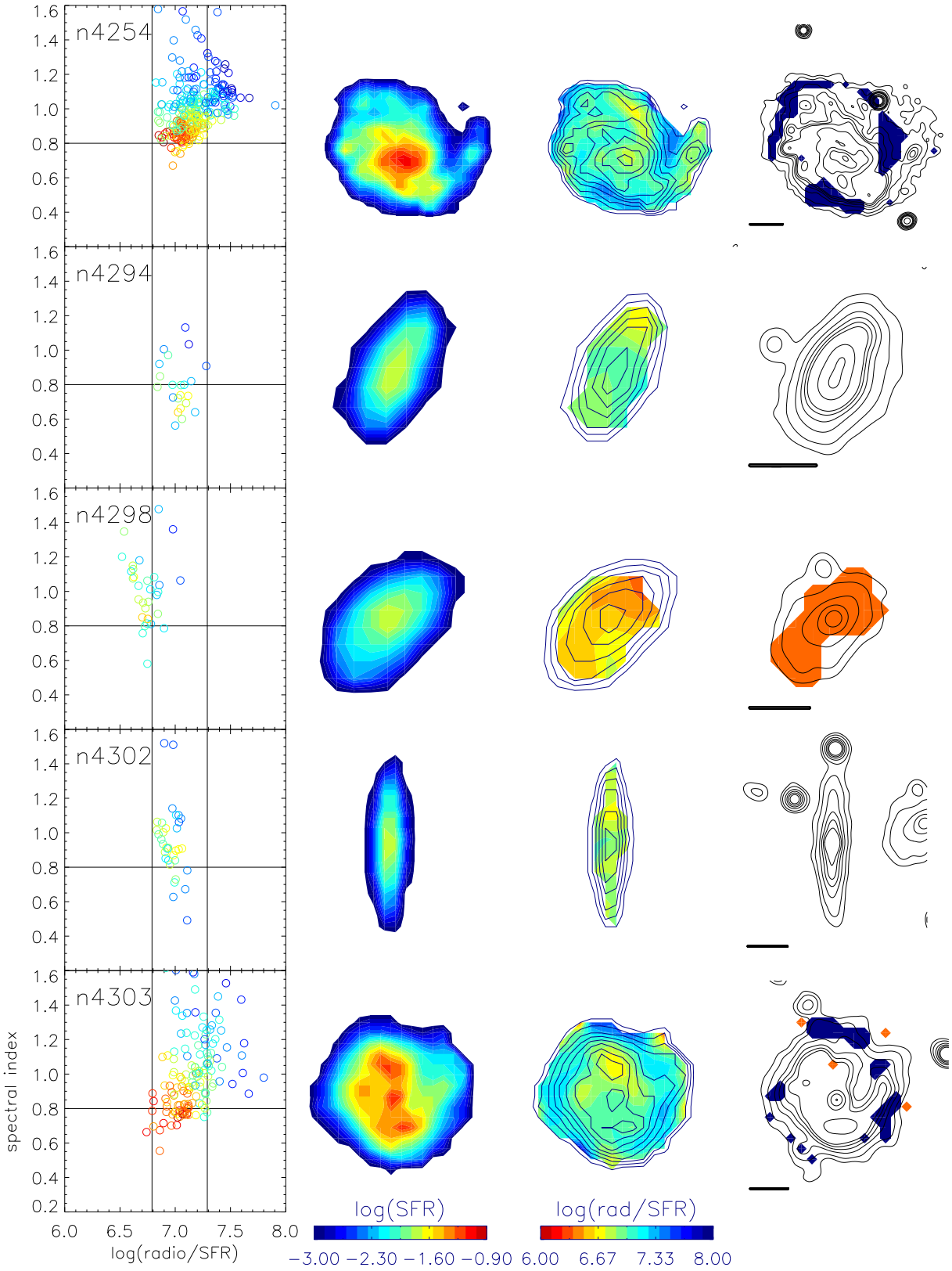

Fig. C.1. As Fig. 3, but the radio continuum contour levels are $(1, 2, 4, 6, 8, 10, 20, 30, 40, 50) \times \xi$ with $\xi = 70$ μJy/beam for NGC 4254 and NGC 4294, $\xi = 150$ μJy/beam for NGC 4298 and NGC 4302, and $\xi = 250$ μJy/beam for NGC 4303.

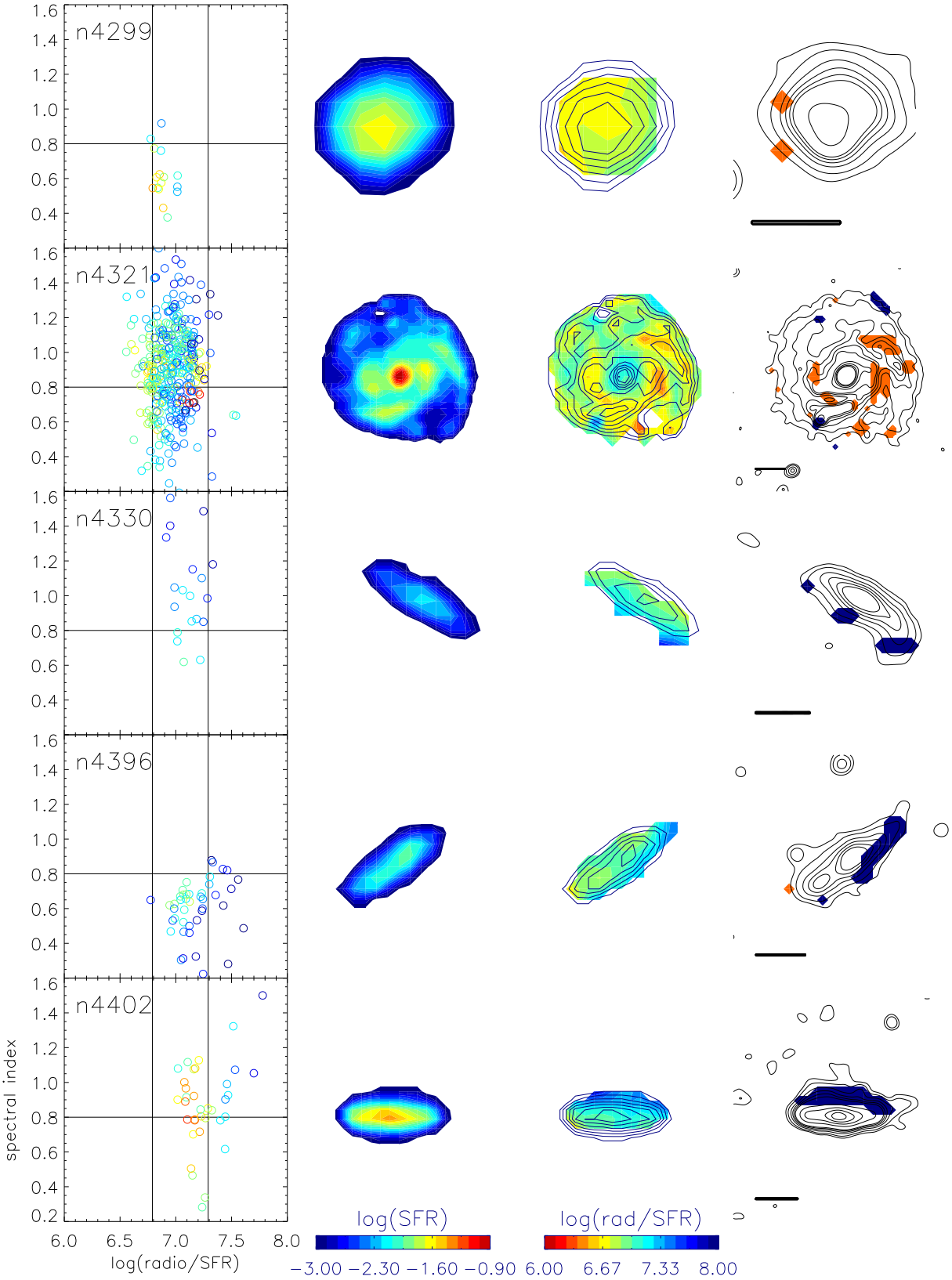

Fig. C.2. As Fig. 3, but the radio continuum contour levels are $(1, 2, 4, 6, 8, 10, 20, 30, 40, 50) \times 70$ μJy/beam.

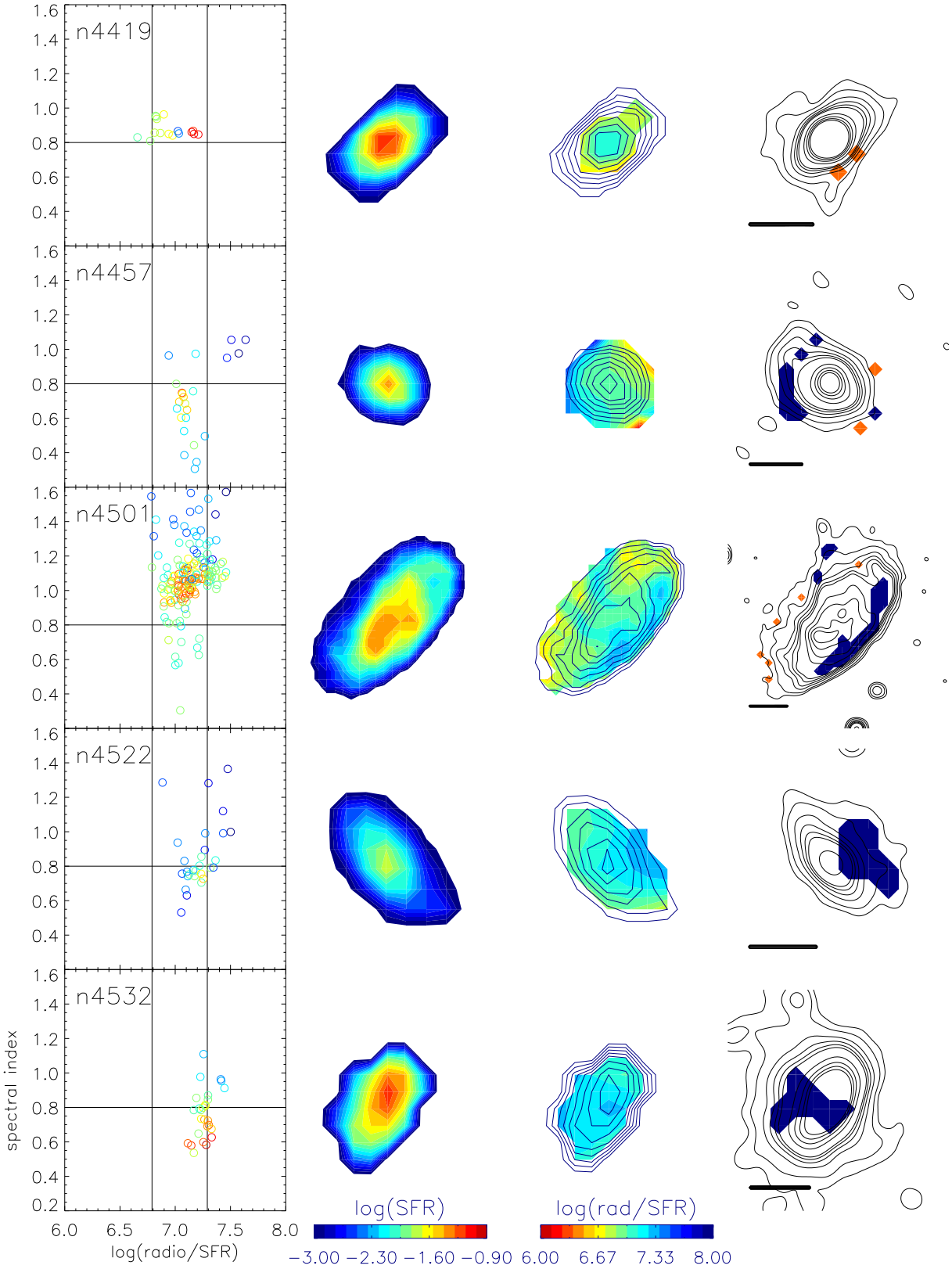

Fig. C.3. As Fig. 3, but the radio continuum contour levels are $(1, 2, 4, 6, 8, 10, 20, 30, 40, 50) \times 70$ μJy/beam.

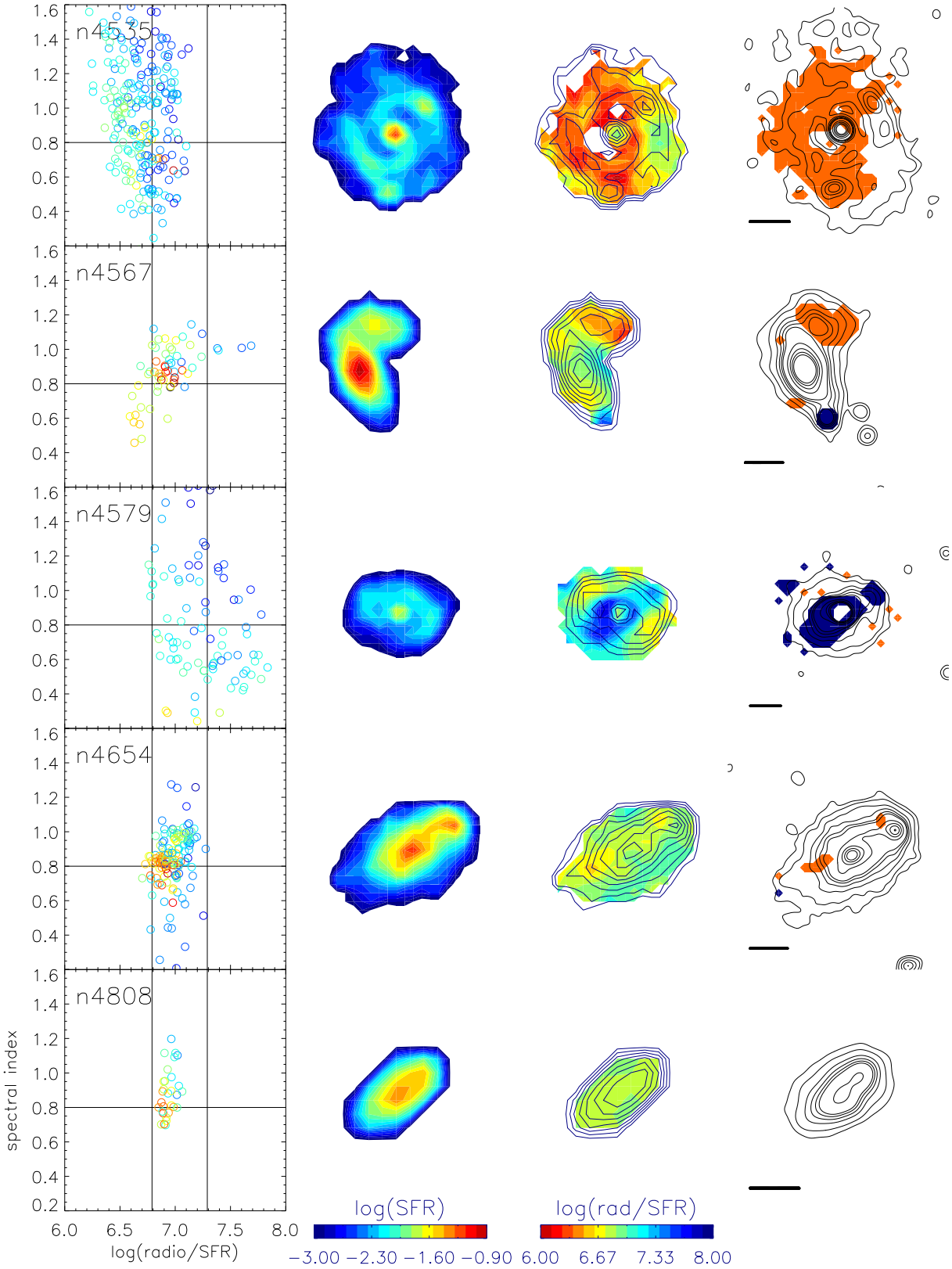

Fig. C.4. As Fig. 3, but the radio continuum contour levels are $(1, 2, 4, 6, 8, 10, 20, 30, 40, 50) \times \xi$ with ξ = 70 μJy/beam for NGC 4535 and NGC 4654 and ξ = 100 μJy/beam for NGC 4567/68, ξ = 150 μJy/beam for NGC 4579 and NGC 4808.

Appendix D: 1.4 GHz data

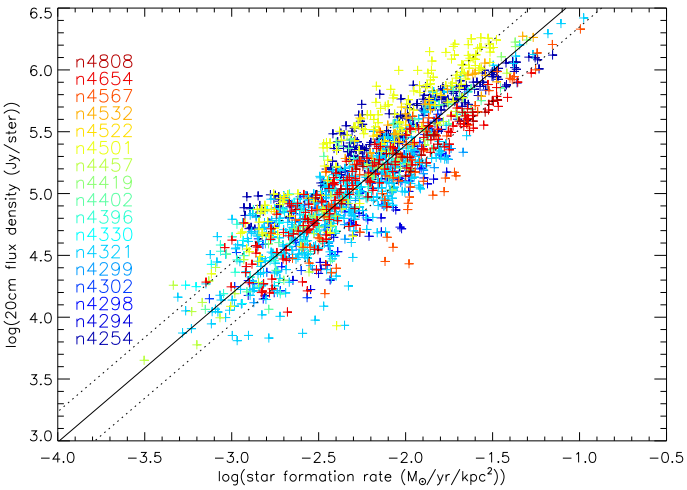

Fig. D.1. As Fig. 2, but for the 1.4 GHz data.

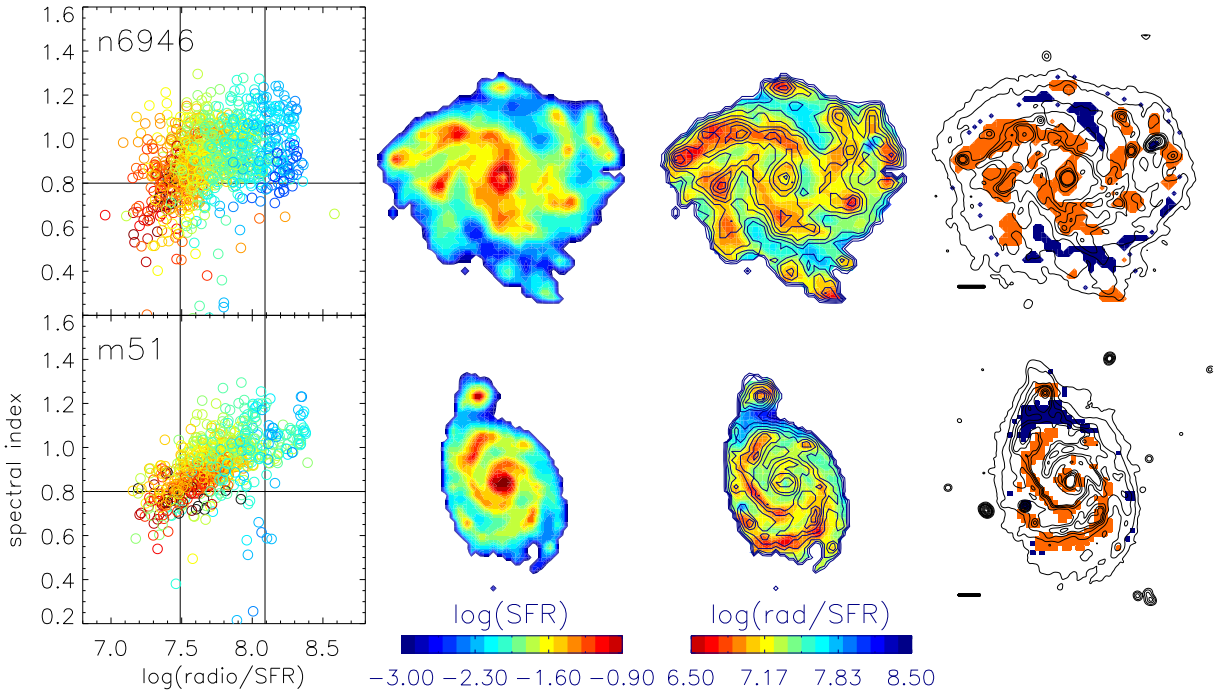

Fig. D.2. As Fig. 3, but for the 1.4 GHz data. The radio continuum contour levels are $(1, 2, 4, 6, 8, 10, 20, 30, 40, 50) \times 1200$ μJy/beam.

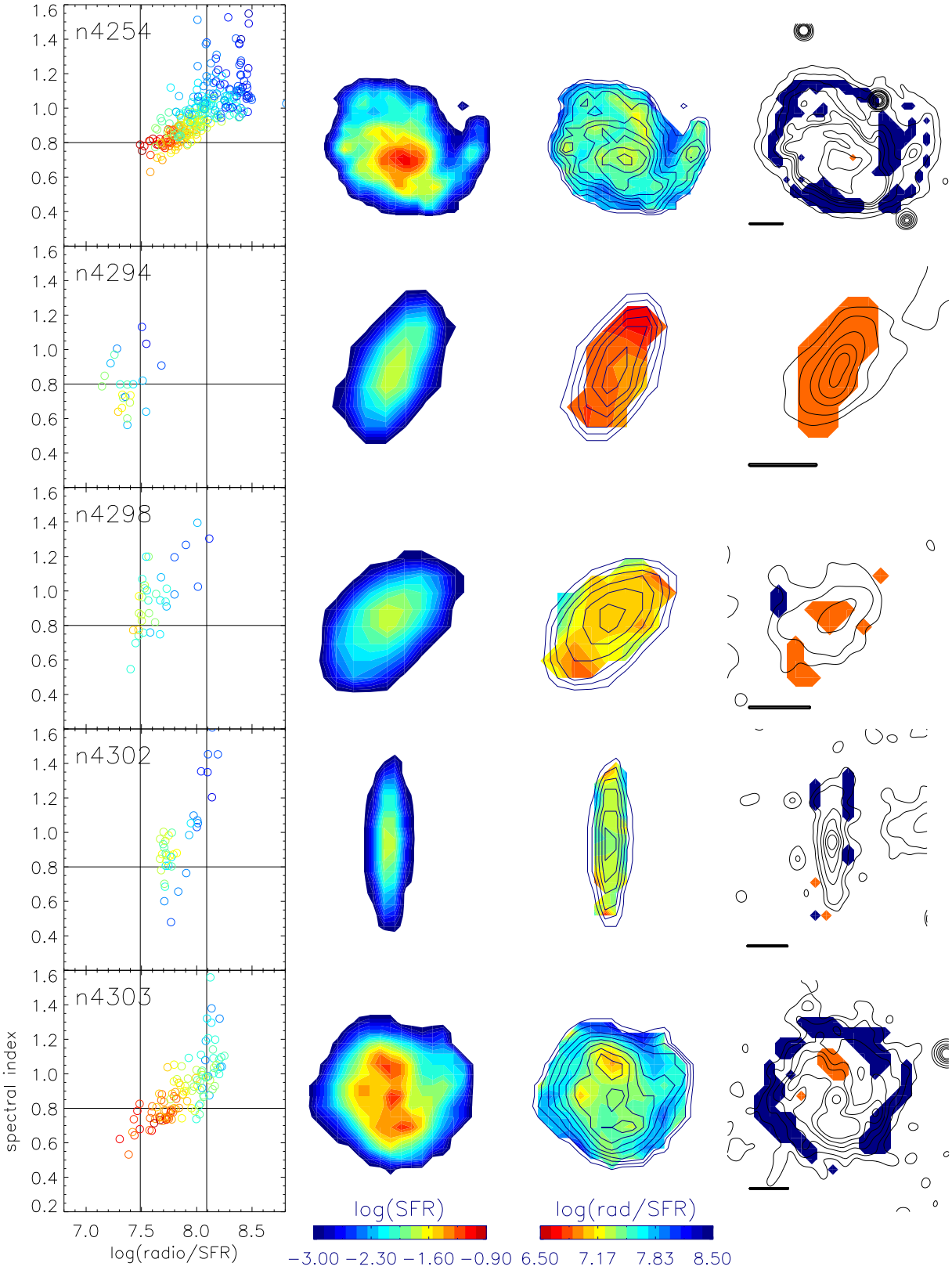

Fig. D.3. As Fig. 3, but for the 1.4 GHz data. The radio continuum contour levels are $(1, 2, 4, 6, 8, 10, 20, 30, 40, 50) \times \xi$ with $\xi = 280$ μJy/beam for NGC 4254 and NGC 4294, $\xi = 600$ μJy/beam for NGC 4298 and NGC 4302, and $\xi = 1000$ μJy/beam for NGC 4303.

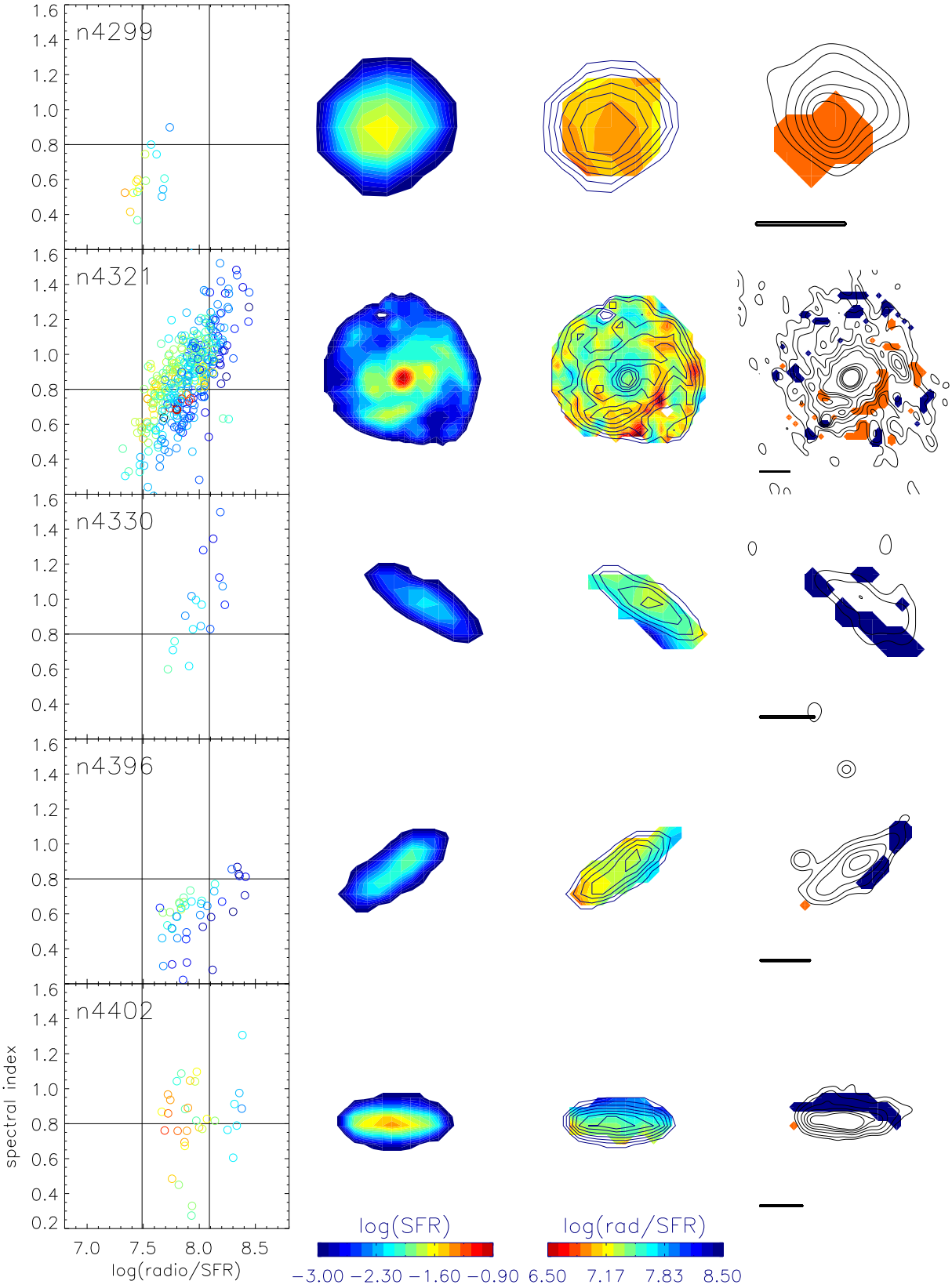

Fig. D.4. As Fig. 3, but for the 1.4 GHz data. The radio continuum contour levels are $(1, 2, 4, 6, 8, 10, 20, 30, 40, 50) \times 280$ μJy/beam.

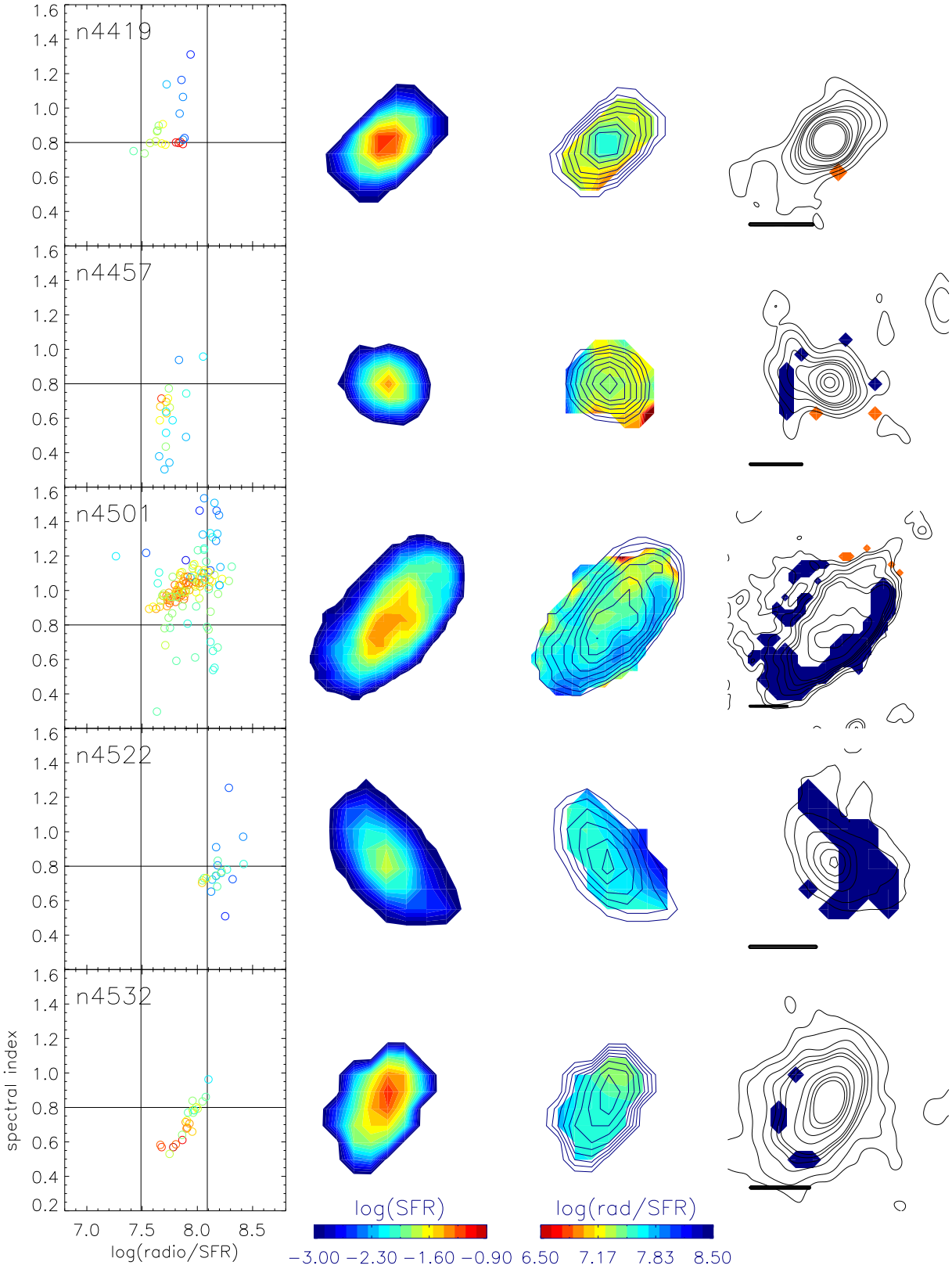

Fig. D.5. As Fig. 3, but for the 1.4 GHz data. The radio continuum contour levels are $(1, 2, 4, 6, 8, 10, 20, 30, 40, 50) \times 280$ μJy/beam.

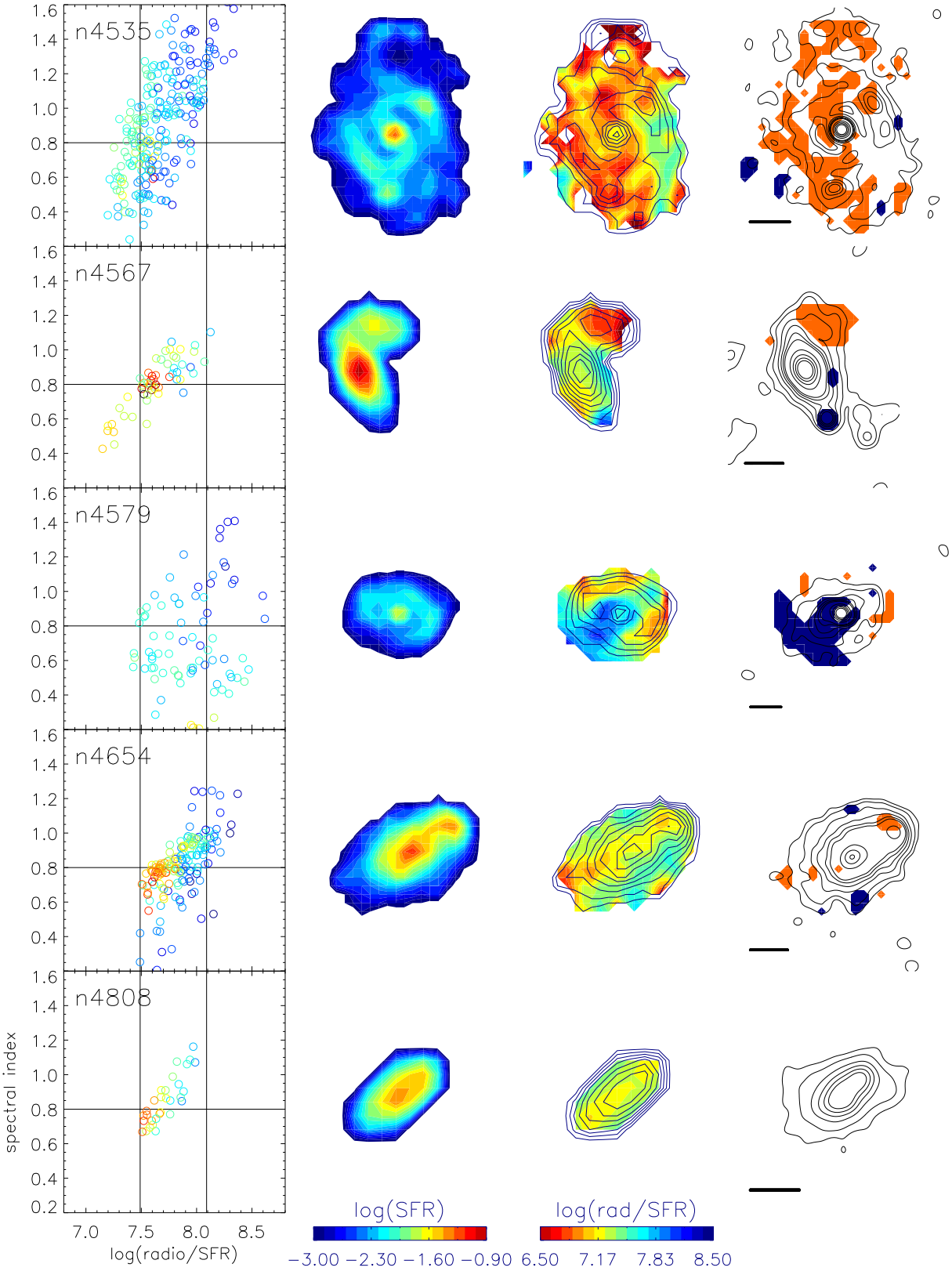

Fig. D.6. As Fig. 3, but for the 1.4 GHz data. The radio continuum contour levels are $(1, 2, 4, 6, 8, 10, 20, 30, 40, 50) \times \xi$ with $\xi = 280$ μJy/beam for NGC 4535 and NGC 4654 and $\xi = 400$ μJy/beam for NGC 4567/68, $\xi = 600$ μJy/beam for NGC 4579 and NGC 4808.

Appendix E: NGC 4579

The radio-bright region in NGC 4579 (Fig. C.4) is tilted by about 40° with respect to the galaxy's major axis, which approximately has an east–west orientation (Chung et al. 2009). The outer parts of the radio-bright regions correspond to the outer spiral arms, which are barely visible in the UV and Hα line. NGC 4579 harbors a gas-rich nuclear spiral (García-Burillo et al. 2005) with a high SFR, which is radio-normal, and an active galactic nucleus (AGN). Whereas the major axis of the HI velocity field coincides with the photometric major axis of the galaxy, the major axis of the ionized gas velocity field within 0.5′ is tilted by ∼ 50° with respect to the HI kinematic major axis (Daigle et al. 2006; Dumas et al. 2007). This tilt roughly corresponds to that of the radio-bright region with respect to the galaxy's major axis. On the other hand, the stellar kinematic major axis within 0.5′ corresponds to the HI kinematic major axis (Dumas et al. 2007). Since the galaxy rotates counter-clockwise, the southern half of the disk is far side. If the inner ionized gas velocity field is produced by streaming motions within the disk, the gas should have a strong outward radial velocity component, whereas inflow is expected within the inner disk region (García-Burillo et al. 2009).

It is surprising that the magnetic field within 0.5′ has the same orientation as the kinematic major axis of the ionized gas (Vollmer et al. 2013), which might be reminiscent of a vertical outflow. An outflow starting in the galactic disk plane would produce negative radial velocities south of the galaxy center. Since this is not observed for the ionized thermal gas, this possibility can be discarded. However, if the outflow is driven by the AGN, the inclination angle of the inner AGN disk can be different from the galactic disk inclination. Given that the observed magnetic field lines would be oriented parallel to the putative AGN-driven outflow, we prefer this scenario. The relatively flat spectral indices found in the radio-bright region, which are close to the injection index of −0.5 (Fig. C.4), are consistent with this interpretation (see Hummel et al. 1989 for NGC 4258).

Appendix F: Correlations

Following Leroy et al. 2008 an SFR uncertainty of 0.2 dex was assumed. We obtained the relations between the SFR and (i) radio continuum, (ii) polarized emission (PI), and (iii) fractional polarization (FP) and (iv) the radio continuum emission and the polarized emission for the 10 largest spiral galaxies with low inclination angles: NGC 6946, M 51, NGC 4254, NGC 4303, NGC 4321, NGC 4501, NGC 4535, NGC 4567/68, NGC 4579, and NC 4654. The disks of NGC 4254 and NGC 4501 were divided into northern and southern halves because the latter contain regions of compressed ISM. A common Spearman correlation coefficient and slope were calculated for all sample galaxies except NGC 4579, where the radio/SFR ratio with respect to PI behaves very much differently from those of the other galaxies (Table F.2). For consistency, the resolution elements of NGC 6946 and M 51 were taken to be 1.5 kpc as for the Virgo cluster galaxies.

As expected, the tightest overall correlations were found for the SFR–radio relation, followed by the SFR–FP, radio–FP, and radio–PI relations. The SFR–PI correlation is moderate ($0.4 \leq \rho < 0.6$) for NGC 4254, NGC 4321, NGC 4501, NGC 4535, and NGC 4579. It is strong ($\rho \geq 0.6$) for NGC 4567/68. On the other hand, NGC 6946, M 51, NGC 4303, and NGC 4654 show no ($\rho < 0.2$) or only a weak SFR–PI correlation ($0.2 \leq \rho < 0.4$). The correlation strength is not linked to perturbations: M 51 and NGC 4567/68 are gravitationally interacting systems with very different SFR–PI Spearman correlation coefficients. Moreover, NGC 4654 and NGC 4501 are both affected by ICM ram pressure and show very different SFR–PI Spearman correlation coefficients. NGC 4321 and NGC 4303 have quite symmetric disks but also have different SFR–PI Spearman correlation coefficients.

All galaxies except NGC 4654 show moderate to strong radio–PI correlations. The associated Spearman correlation coefficients are significantly higher than those of the SFR–PI correlation. Overall, the radio–PI relations are steeper than the SFR–PI relations of our sample galaxies. However, there are exceptions: the southern disk halves of NGC 4254 and NGC 4567/68. A tighter radio–PI than SFR–PI correlation is expected because the same relativistic electron population is responsible for the PI and radio emission. The relatively strong anticorrelations between SFR and FP on the one hand, and radio and FP (not separately presented because it is not a fundamental relation) on the other hand are driven by the SFR–radio correlation. The radio emission most closely related to recent star formation has low polarization because of tangled/irregular magnetic fields. It is remarkable that the SFR–FP correlations are slightly stronger than the radio–FP correlations in most of the galaxies. As expected from the shallower SFR–PI relations with respect to the radio–PI relations, the SFR–FP relations are generally steeper than the radio–FP relations.

Table F.1. Spearman rank correlation coefficients.

x-axis – y-axis	log(SFR)– log(radio[(a)])	log(SFR)– log(PI[(b)])	log(SFR)– log(FP[(c)])	log(radio)– log(PI)	log(SFR)– log(radio/SFR)	log(PI)– log(radio/SFR)	log(FP)– log(radio/SFR)
NGC6946	0.74	(0.16)	-0.64	0.41	-0.68	(0.21)	(0.30)
M51	0.69	(0.29)	-0.60	0.56	(-0.35)	0.41	(-0.04)
NGC4254s	0.95	0.41	-0.86	0.56	-0.52	(0.36)	0.65
NGC4254n	0.89	0.45	-0.84	0.55	-0.77	(-0.08)	0.61
NGC4303	0.94	0.32	-0.85	0.48	(-0.34)	0.50	(0.29)
NGC4321	0.91	0.50	-0.81	0.67	(-0.17)	0.41	(0.11)
NGC4501s	0.96	0.51	-0.65	0.70	(-0.04)	0.62	(0.28)
NGC4501n	0.96	0.53	-0.74	0.60	(-0.04)	(0.32)	(0.14)
NGC4535	0.72	0.47	-0.84	0.59	(0.20)	0.41	(-0.29)
NGC4567/68	0.79	0.62	-0.77	0.73	(0.19)	0.57	(-0.37)
NGC4579	0.84	0.42	-0.79	0.70	(-0.02)	0.52	-0.47
NGC4654	0.96	(-0.03)	-0.93	(-0.02)	-0.65	(0.05)	0.55
total[(d)]	0.86	(0.39)	-0.76	0.60	(-0.29)	0.41	(0.14)

(a) nonthermal (synchrotron) radio continuum emission; (b) surface brightness of polarized radio continuum emission (PI); (c) fractional polarization (FP); (d) correlation for data from all galaxies except NGC 4579

Table F.2. Slopes of the linear fits.

x-axis– y-axis	log(SFR)– log(radio)	log(SFR)– log(PI)	log(SFR)– log(FP)	log(radio)– log(PI)	log(SFR)– log(radio/SFR)	log(PI)– log(radio/SFR)	log(FP)– log(radio/SFR)
NGC6946	0.86 ± 0.03	(0.19 ± 0.03)	−0.67 ± 0.04	0.42 ± 0.03	−0.49 ± 0.03	(0.22 ± 0.04)	(0.24 ± 0.03)
M51	1.06 ± 0.04	(0.35 ± 0.04)	−0.76 ± 0.04	0.42 ± 0.02	(−0.39 ± 0.04)	0.36 ± 0.04	(−0.10 ± 0.03)
NGC4254s	0.93 ± 0.05	0.34 ± 0.08	−0.82 ± 0.06	0.40 ± 0.06	−0.18 ± 0.07	(0.23 ± 0.10)	0.28 ± 0.08
NGC4254n	0.85 ± 0.03	0.21 ± 0.05	−0.65 ± 0.05	0.28 ± 0.05	−0.34 ± 0.06	(−0.14 ± 0.16)	0.37 ± 0.08
NGC4303	1.02 ± 0.04	(0.24 ± 0.05)	−0.85 ± 0.05	0.32 ± 0.04	(−0.15 ± 0.05)	0.33 ± 0.07	(0.07 ± 0.04)
NGC4321	1.09 ± 0.03	0.83 ± 0.07	−0.83 ± 0.04	0.46 ± 0.03	(−0.01 ± 0.05)	0.38 ± 0.07	(−0.02 ± 0.05)
NGC4501s	1.25 ± 0.07	0.79 ± 0.20	−0.85 ± 0.16	0.63 ± 0.09	(0.06 ± 0.11)	0.30 ± 0.09	(0.08 ± 0.10)
NGC4501n	1.12 ± 0.04	0.55 ± 0.15	−0.78 ± 0.14	0.48 ± 0.09	(−0.34 ± 0.06)	(0.12 ± 0.12)	(0.05 ± 0.11)
NGC4535	1.20 ± 0.07	0.05 ± 0.15	−1.12 ± 0.18	0.15 ± 0.08	(0.11 ± 0.21)	0.50 ± 0.56	(−0.14 ± 0.14)
NGC4567/68	1.15 ± 0.10	0.64 ± 0.16	−0.85 ± 0.16	0.44 ± 0.07	(0.08 ± 0.17)	0.35 ± 0.22	(−0.23 ± 0.17)
NGC4579	1.44 ± 0.11	0.43 ± 0.09	−1.15 ± 0.13	0.34 ± 0.03	(0.02 ± 0.13)	1.08 ± 0.15	−0.48 ± 0.07
NGC4654	0.95 ± 0.05	(−0.03 ± 0.07)	−0.98 ± 0.09	(−0.02 ± 0.07)	−0.15 ± 0.09	(0.16 ± 0.42)	0.13 ± 0.09
total[(a)]	1.11 ± 0.02	(0.43 ± 0.03)	−0.83 ± 0.02	0.41 ± 0.02	(−0.19 ± 0.02)	0.31 ± 0.03	(0.05 ± 0.02)

All slopes with an associated Spearman correlation coefficient $|\rho| < 0.4$ are in brackets. (a) correlation for data from all galaxies except NGC 4579

Appendix G: The PI–radio/SFR relation

Based on the SFR–PI and radio–PI relations, we expect a slope of the log(PI)–log(radio/SFR) relation of $1/0.41 - 1/0.43 = 0.11 \pm 0.20$. The observationally derived log(PI)–log(radio/SFR) slope of 0.31 ± 0.03 is thus consistent within 1σ with the expected value. The fact that it is located at the higher end of the expected range can be explained in the following way: the slopes of the log(PI)–log(SFR) and log(PI)–log(radio) relations calculated with the Bayesian approach are 0.65 ± 0.05 and 0.96 ± 0.04, respectively. These are not the inverse of the log(SFR)–log(PI) and log(radio)–log(PI) relations because of a significant number of resolution elements with high PI and relatively high SFR or radio continuum emission (Fig. G.1). These points are more relevant for the fitting of the log(PI)–log(SFR) and log(PI)–log(radio) relations than for the fitting of the log(SFR)–log(PI) and log(radio)–log(PI) relations. The PI–radio/SFR correlation is thus driven by regions of high PI in the interacting galaxies.

The log(PI)–log(radio/SFR) slope is consistent with the log(PI)–log(radio) and log(PI)–log(SFR) slopes $0.96 - 0.65 = 0.31 \pm 0.06$. Remarkably, the resulting log(radio/SFR)–log(PI) and log(PI)–log(radio/SFR) have consistent slopes of 3.24 ± 0.24 and 0.31 ± 0.02, respectively (Table F.2 and Fig. G.1). This makes us confident that the PI–radio/SFR correlation is meaningful.

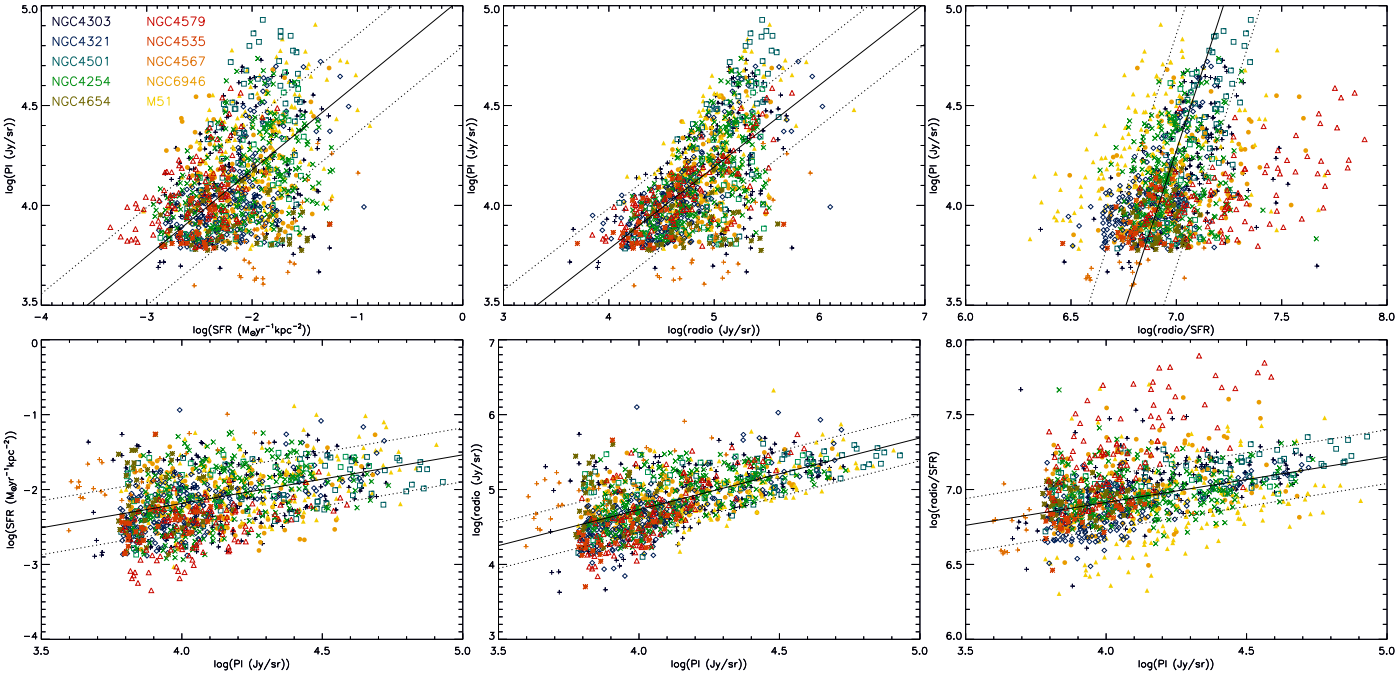

Fig. G.1. Correlations involving polarization. From upper left to lower right: log(SFR)–log(PI), log(radio)–log(PI), log(radio/SFR)–log(PI), log(PI)–log(SFR), log(PI)–log(radio), and log(PI)–log(radio/SFR) relations. The lines show the linear fits (solid) and scatter (dotted). NGC 4579 was excluded from the linear regression.

Appendix H: Interpretation of the SFR–radio and the SFR–FP correlations

The mean slope of the log(SFR)–log(radio) correlation is 1.11 ± 0.02 (Table F.2). In the case of CR and magnetic field energy equipartition (Beck & Krause 2005), a typical synchrotron spectral index of −0.8, and $B_{\rm tot} \propto SFR^{0.3}$ (Heesen et al. 2014), we obtained for the radio continuum emission $I_\nu \propto B_{\rm tot}^{3.8} \propto SFR^{1.3}$, which is very close to the measured value. The slopes of the individual galaxies significantly vary from 0.85 to 1.44. This behavior might be due to (i) a variation of the spectral index from galaxy to galaxy, (ii) CR–magnetic field equipartition is not always valid, (iii) the exponent of the $B_{\rm tot}$–SFR relation varies from galaxy to galaxy, (iv) CR diffusion reduces the contrast in radio continuum with respect to the contrast in SFR, or (v) galaxies with high SFR or magnetic field are closer to the CRe calorimeter condition where the slope should be close to unity. In addition, CR diffusion is less relevant because the diffusion length becomes shorter with increasing magnetic field strength. Anticipating our model results of Sect. 4.4.1, we found the following model SFR–radio slopes: 1.08 for the calorimeter model $t_{\rm eff} = t_{\rm sync}$, 0.89 for a model without CR diffusion including bremsstrahlung, IC, ion, and pion losses, and 0.73 for a model including CR diffusion. Thus both, energy losses (bremsstrahlung, IC, ion, and pion) and CR diffusion lead to shallower SFR–radio slopes.

Since the mean spectral index of our sample galaxies varies from −0.57 to −1.03 and $I_\nu \propto \nu^{-\alpha} B^{3+\alpha} \propto SFR^{0.9+0.3\alpha}$, the expected slopes range between 1.07 and 1.21. The inspection of the relation between the log(SFR)–log(radio) slope and the mean SI (left panel of Fig. H.2) shows that only NGC 4501 shows the expected behavior for item (i). Anticipating the results of our modeling (Sect. 4), diffusion can lead to a flattening of the log(SFR)–log(radio) slope by 0.2. Thus, item (iv) is potentially relevant in all galaxies. Moreover, the relation between the log(SFR)–log(radio) slope and the SFR (right panel of Fig. H.2) suggests that item (v) is also relevant in most of the galaxies.

We conclude that items (i), (iv), and (v) contribute to the galaxy-to-galaxy variation of the log(SFR)–log(radio) slope; items (ii) and (iii) cannot be ruled out.

The SFR–radio correlation is much steeper and tighter than the SFR–PI correlation. This results in an SFR–FP anticorrelation. We thus observe a degree of magnetic field anisotropy or field ordering (anisotropy), which decreases with increasing SFR. This can be interpreted by three mechanisms: (i) the large-scale dynamo operates preferably in regions with low SFR (see, for example, Beck et al. 2019). In addition, regular fields are tangled and thus destroyed in regions of higher SFR. (ii) Compression and shear of isotropic random fields, which lead to field ordering (anisotropy), mainly occur in regions with low SFR where the gas energy density is also low. In regions of high SFR, magnetic and kinetic energy densities are too high to be significantly affected by compression and shear (see Eqs. 7 and 8). (iii) Faraday depolarization is expected to be stronger in regions of high SFR leading to lower PI at high SFR.

For high dispersions in rotation measure ($\sigma_{\rm RM} \gtrsim 300$ rad m^{-2}) the degree of polarization varies with $\sigma_{\rm RM}^{-2} \sim (< n_{\rm e} > B_{\rm turb})^{-2}$, where $n_{\rm e}$ is the density of thermal electrons along the line of sight (see, for example, Eq. 13 of Beck 2015 or Eq. 34 of Sokoloff et al. 1998). It is thus expected that the log(SFR)–log(FP) slope becomes smaller with increasing SFR. Since this is not observed (Fig. H.3), we conclude that Faraday depolarization does not play a role for the SFR–FP correlation. An apparent opposite effect is caused by NGC 4579, NGC 4535, and NGC 4654. The steep SFR–FP correlations of NGC 4535 and NGC 4654 (fourth column of Table F.2) are due to a high FP in regions of low SFR caused by interaction-induced shear motions. In NGC 4579 the steepness of the correlation is driven by a low FP in the radio-bright region. We speculate that this is due to an intrinsically small FP of the emission from the nuclear disk and the AGN and some beam depolarization (outflow versus disk field).

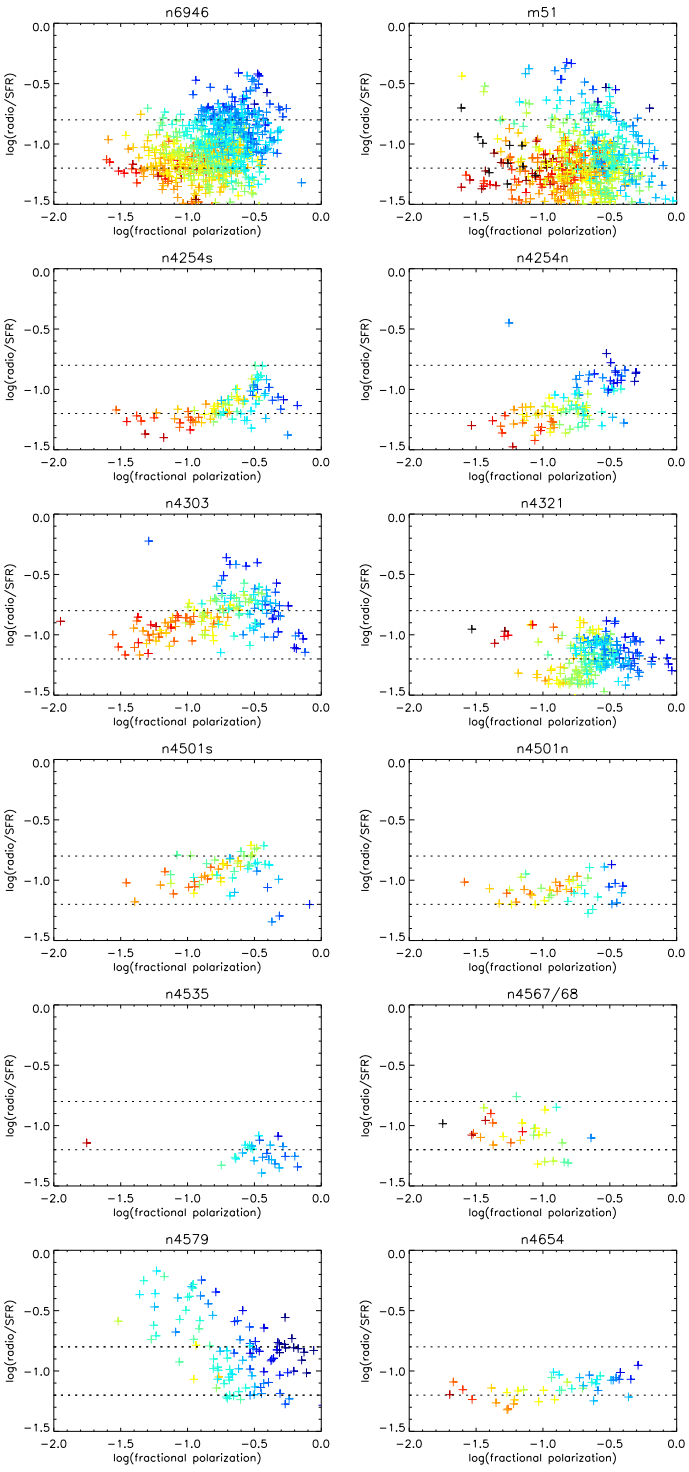

Fig. H.1. Ratio between the radio surface brightness and the star formation rate per unit area as a function of the fractional polarization. The colors correspond to the star formation rate per unit area; see Fig. 3 for the color scale.

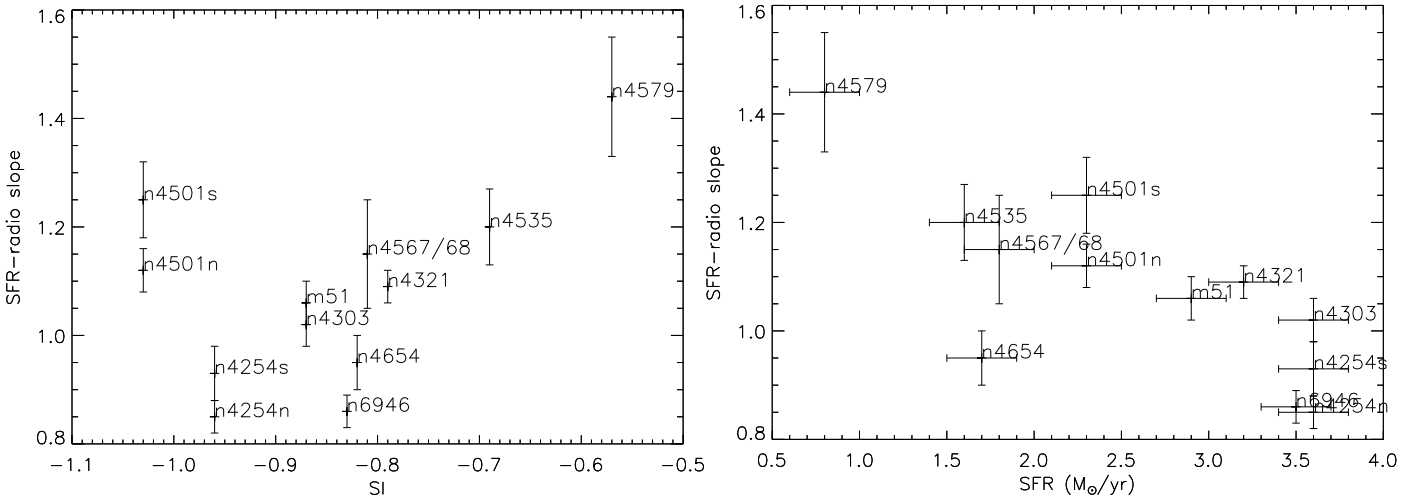

Fig. H.2. Slope of the log(SFR)–log(radio) correlation (from Table F.2, column 2) as a function of the mean spectral index (left) and the SFR (right).

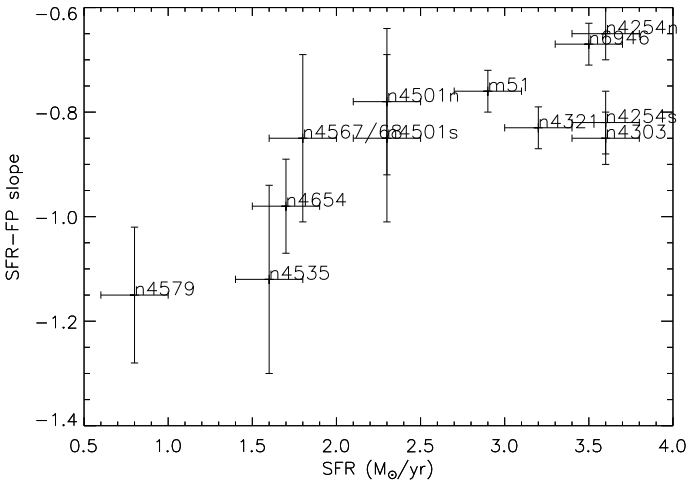

Fig. H.3. Slope of the log(SFR)–log(FP) correlation (from Table F.2, column 4) as a function of the SFR.

NGC 6946 is the only isolated galaxy in our sample. Its SFR–FP correlation coefficient is not different from that of the other galaxies. However, the slope of the correlation is significantly steeper for the interacting galaxies than for NGC 6946. We suggest that while the SFR–FP correlation in all galaxies is driven by mechanism (i), the steeper slopes are caused by mechanism (ii).

Appendix I: Additional model calculations

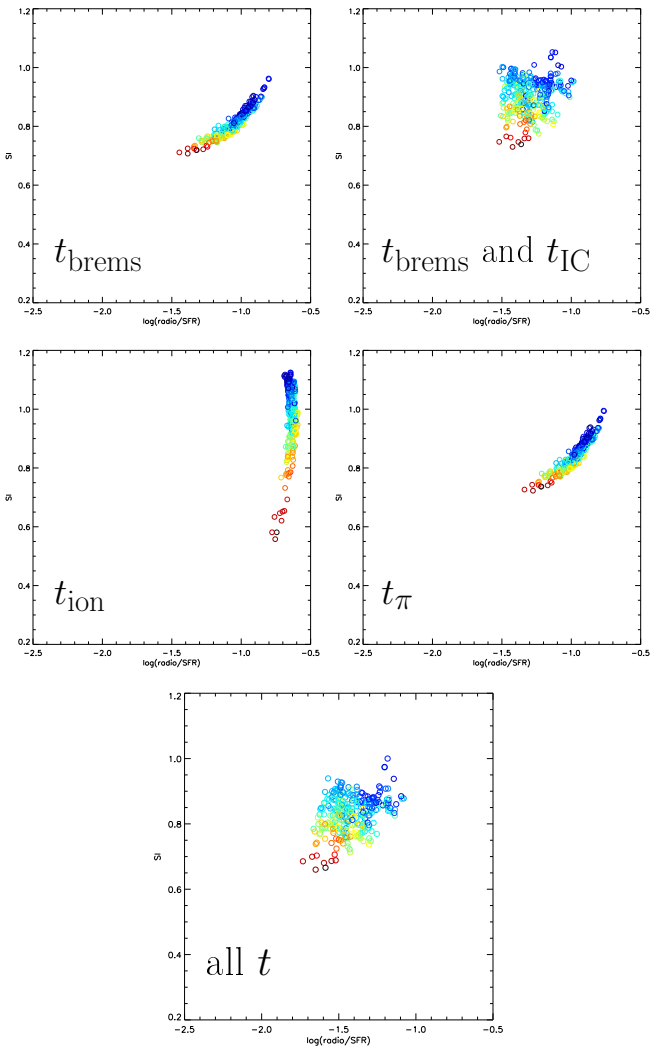

Fig. I.1. Spectral index as a function of the ratio between the radio continuum surface brightness and the star formation rate per unit area. The effective timescale contains the timescales that are marked on the plots.

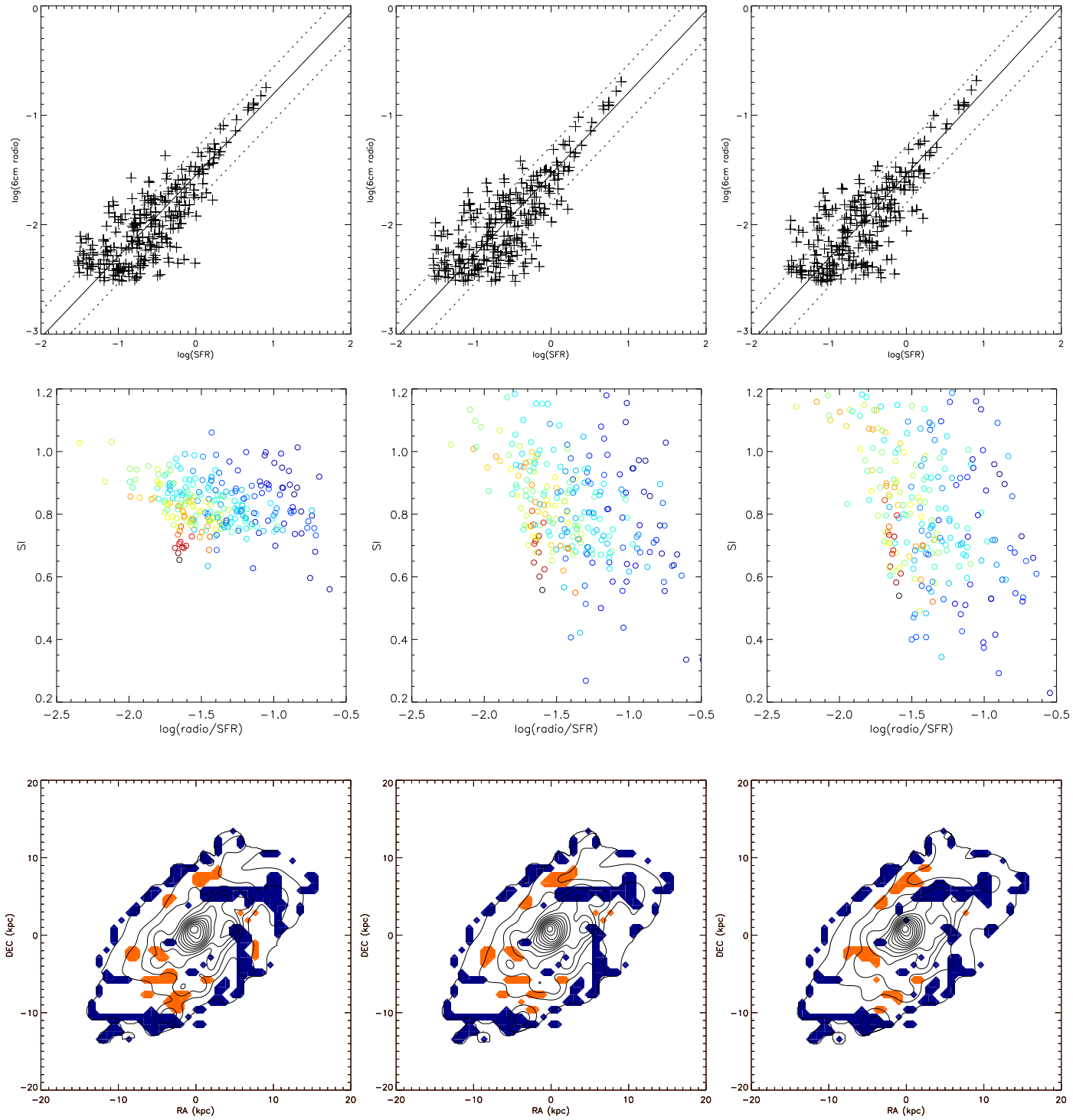

Fig. I.2. As Fig. 7. Left panel: with an energy-dependent diffusion coefficient $D = D_0 = 10^{28}$ cm^{2}s^{-1} for $E \leq 3$ GeV and $D = D_0(E/(3\,\mathrm{GeV}))^{0.3}$ for $E > 3$ GeV. Middle panel: with $D = 2 \times D_0$ for all energies. Right panel: with $D_0 = 2 \times 10^{28}$ cm^{2}s^{-1} and an energy-dependent diffusion coefficient.

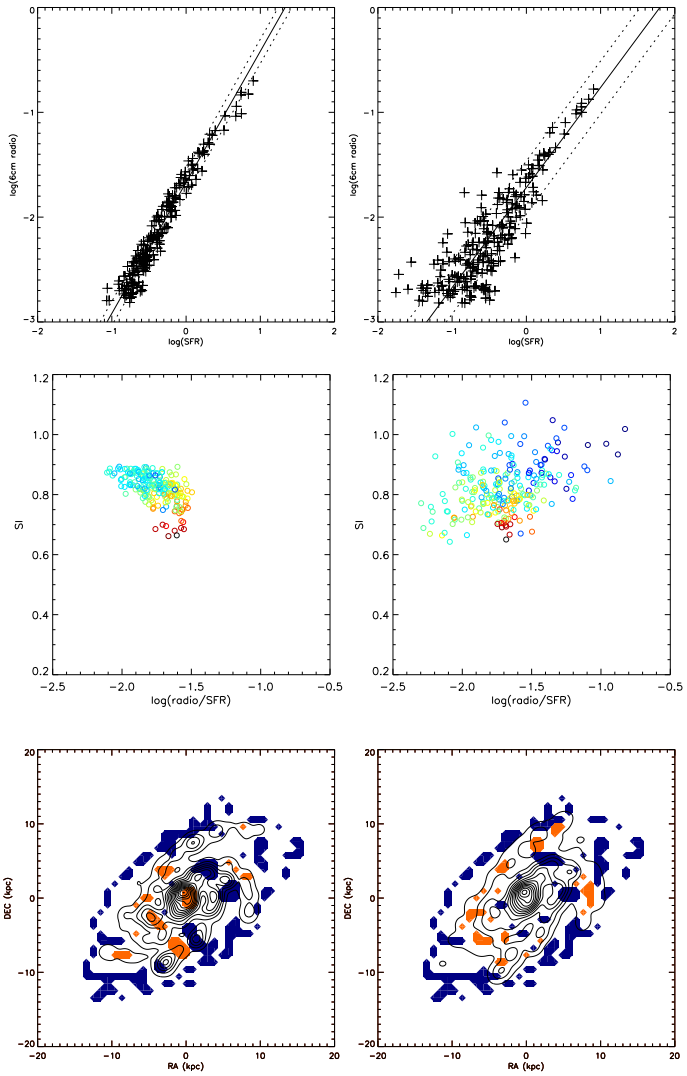

Fig. I.3. As Fig. 7, but with additional diffusive escape: $t_{\rm eff}^{-1} = (t_{\rm sync}^{-1} + t_{\rm brems}^{-1} + t_{\rm IC}^{-1} + t_{\rm ion}^{-1} + t_{\pi}^{-1} + t_{\rm escp}^{-1})^{-1}$.

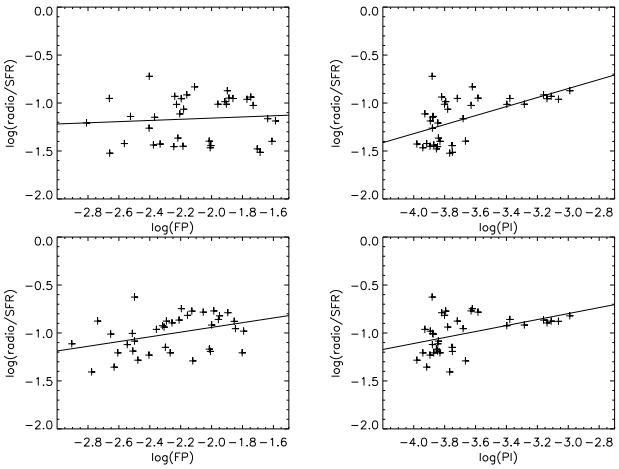

Fig. I.4. NGC 4501 model log(radio/SFR)–FP (left panels) and log(radio/SFR)–PI relations (right panels). The upper panels correspond to Fig. 8. Lower panels: addition of a regular field component $B_{\rm reg} = 12\ \mu$G in regions of enhanced model polarized intensity (cf. Fig. 9).